Pressure-induced structural and electronic transitions in kesterite-type Cu_2ZnSnS_4

Ilias Efthimiopoulos,[1, a)] Tim Küllmey,[2] Sergio Speziale,[1] Anna S. Pakhomova,[3] Marcel Quennet,[2,4] Beate Paulus,[2] Anna Ritscher,[4,5] Martin Lerch,[5] and Monika Koch-Müller[1]

[1)] *GFZ German Research Centre for Geosciences, Telegrafenberg, 14473 Potsdam, Germany*

[2)] *Institut für Chemie und Biochemie, Freie Universität Berlin, Takustr. 3, 14195 Berlin, Germany*

[3)] *PETRA III, Deutsches Elektronen Synchrotron, 22607 Hamburg, Germany*

[4)] *Helmholtz-Zentrum Berlin für Materialien und Energie, Hahn-Meitner-Platz 1, 14109 Berlin, Germany*

[5)] *Institut für Chemie, Technische Universität Berlin, Strasse des 17.Juni 135, 10623 Berlin, Germany*

(Dated: 10 August 2018)

We have performed structural investigations of ordered kesterite-type Cu_2ZnSnS_4 up to 30 GPa. Our current X-ray diffraction results clearly excluded the presence of a kesterite→disordered kesterite transition reported earlier between 7-9 GPa. Nevertheless, specific anomalies connected with the Cu-S bond length of the starting kesterite-type phase are evidenced close to 6 GPa, indicating subtle structural effects at play in this system. Moreover, we have indexed the high-pressure modification of Cu_2ZnSnS_4 adopted above 16 GPa to a disordered GeSb-type structure, a tetragonally distorted rocksalt-type modification. Full decompression leads to the adoption of a disordered sphalerite/zincblende-type structure. Our complementary density functional theory calculations reproduce accurately the experimental observations and indicate the possibility of a metallic high-pressure GeSb-type phase, unlike the starting semiconducting kesterite-type Cu_2ZnSnS_4 structure.

I. INTRODUCTION

The impending exhaustion of fossil fuel has prompted the exploration and exploitation of alternative energy resources, with the solar energy harvesting through photovoltaic devices spearheading these efforts. In an attempt to overcome the restraints of silicon-based materials, the direct optical band gap (E_g) of chalcogenide-bearing solar cells offers the benefit of higher absorption in comparison to silicon. Among the various chalcogenide compounds investigated for this purpose, the quaternary semiconductor Cu_2ZnSnS_4 has attracted considerable attention in recent years[1,2]. The suitability of this material for solar cell applications stems from its almost optimal band gap ($E_g \approx 1.5$ eV), its high absorption coefficient in the visible energy range ($\sim 10^4$ cm^{-1}), and its earth-abundant, low-cost, and non-toxic elemental constituents[3–5]. Given the fact that the current power conversion efficiency record for Cu_2ZnSnS_4 thin films is $\sim$9%[6], a value which still lies far away from the theoretical limit of $\sim$30%[7], it becomes clear that further investigations are needed for improving the photovoltaic efficiency of Cu_2ZnSnS_4.

At ambient conditions, Cu_2ZnSnS_4 crystallizes in the tetragonal kesterite (KS) structure (space group SG $I\bar{4}$, $Z = 2$, Fig. 1)[8,9]. This phase, which is structurally derived from the sphalerite/zincblende (ZB) structure, and is therefore closely related to the chalcopyrite- and stannite-type phases by altering the metal/cationic ordering[10], is composed of alternating Cu/Sn and Cu/Zn layers along the long c-axis interrupted by sulfur anions, with all of the Cu, Zn, and Sn cations tetrahedrally coordinated with respect to the S anions (Fig. 1). Even though the KS phase represents an ordered cationic arrangement, with each cation occupying a unique Wyckoff site, cationic disorder is quite common in this material[8,11–15]. Such cationic disorder may have notable effects on the photovoltaic properties of Cu_2ZnSnS_4. For example, one of the most common types of cationic disorder in Cu_2ZnSnS_4 is the mixed occupancy between the Cu and Zn sites lying in the z = 1/4 and z = 3/4 cationic layers, which results in a disordered kesterite configuration (SG $I\bar{4}2m$, $Z = 2$, DKS) and a concomitant reduction of the Cu_2ZnSnS_4 band gap E_g by 0.1-0.15 eV[3,16,17].

Both the sensitivity towards cationic disorder, as well as the inherent anisotropy of the tetragonal Cu_2ZnSnS_4 KS structure, strongly imply that the physical and chemical properties of this material are susceptible to external perturbations such as temperature T and pressure P. Indeed, increasing T leads to a KS→DKS transition at ca. 550 K, whereas a DKS→disordered ZB-type structural transition has been observed above 1300 K[9,18–20]. On the other hand, the effect of compression on Cu_2ZnSnS_4 has been only recently investigated. *Ab initio* theoretical studies showed that application of compressive (tensile) stress increases (decreases) the band gap E_g, whereas a transition of the KS phase towards a stannite modification (SG $I\bar{4}2m$, $Z = 2$), which exhibits a different stacking of cationic layers along c-axis compared to the KS phase with alternating layers of tetrahedrally coordinated Zn/Sn and Cu ions, was predicted to take place close to 32 GPa[21–23]. Subsequent high-pressure X-ray diffraction (XRD) experimental investigations, however, contradicted the predicted KS→stannite structural transition. In particular, compression of Cu_2ZnSnS_4 at ambi-

[a)] Electronic mail: iliefthi@gfz-potsdam.de

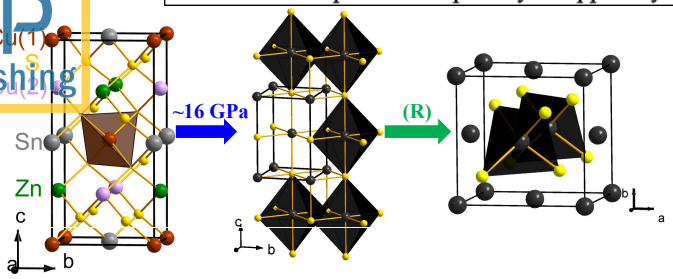

FIG. 1: Structural representations of the ordered ambient-pressure kesterite-type Cu_2ZnSnS_4 phase (SG $I\bar{4}$, $Z = 2$, left), the high-pressure disordered GeSb-type modification adopted close to 16 GPa (SG $I4/mmm$, $Z = 2$, middle), and the disordered sphalerite/zincblende-type polymoph (ZB, SG $F\bar{4}3m$,$Z = 4$, right) adopted upon full pressure release (R). The brown, purple, green, gray, and yellow spheres represent Cu(1), Cu(2), Zn, Sn, and S ions, respectively; the dark spheres in the GeSb-type and ZB-type phases depict the mixed and random Cu/Zn/Sn cationic occupancy. The respective KS→GeSb-type transition pressure is also provided (see also **Table I**).

ent temperature led to a KS→DKS transition between 7-9 GPa, whereas the DKS modification transformed into a disordered rocksalt-type (RS) structure close to 15 GPa; the latter was accompanied by an increase of the respective cationic coordination from fourfold to sixfold[24]. An overview of the reported high-pressure Cu_2ZnSnS_4 modifications is listed in Table I.

Here we have expanded upon the investigation of the pressure-induced structural response of ordered Cu_2ZnSnS_4 up to 30 GPa by means of high-pressure XRD measurements. One of the primary motivations was the re-investigation of the aforementioned KS→DKS transition between 7-9 GPa; given that the previous XRD study was performed with argon serving as a pressure transmitting medium (PTM, Table I), we considered the possibility of non-hydrostatic conditions imposing the KS→DKS transition. Hence, we used neon PTM in a XRD run up to 11.4 GPa. In a nutshell, the neon PTM XRD experiments did not show the KS→DKS transition; following this result, a second XRD experiment performed with argon as PTM did not again yield the KS→DKS transition. Closer inspection of the collected XRD images indicated an argon-related Debye diffraction ring in the first experiment as the origin behind this discrepancy (Fig. S1 and Fig. S2 in the **Supplement**). Moreover, the high-pressure Cu_2ZnSnS_4 modification stable above 14-16 GPa was assigned to a disordered GeSb-type structure (SG $I4/mmm$, $Z = 2$), a tetragonally distorted modification of the previously reported RS-type phase[24]. Upon full decompression, we recovered a disordered ZB-type structure. We have additionally performed density functional theory (DFT) calculations, which reproduced the experimental observations. In addition, the high-pressure GeSb-type phase is predicted to exhibit metallic conductivity, unlike the starting semiconducting KS structure.

II. METHODS

A. Experimental details

The investigated ordered Cu_2ZnSnS_4 sample was available in polycrystalline powder form. Synthesis and characterization details can be found elsewhere[25–27].

Angle-resolved high-pressure XRD measurements were performed at the Extreme Conditions Beamline (ECB) P02.2 of PETRA III (Hamburg, Germany)[28] with an incident X-ray wavelength $\lambda \simeq 0.29$ Å ($E \simeq 43$ keV) and a beam size of 2 μm × 2 μm. Two-dimensional XRD patterns were collected with a fast flat panel detector XRD1621 from PerkinElmer (2048 pixels × 2048 pixels, 200 × 200 μm^2 pixel size) and processed with the FIT2D software[29]. Refinements were performed using the GSAS+EXPGUI software packages[30].

Diamond anvil cells (DACs) equipped with diamonds of 300 μm and 400 μm culet diameters were used for pressure generation. Rhenium gaskets were preindented to a thickness of ∼35 μm, with holes of 150-200 μm diameter acting as sample chambers. Neon and argon served both as pressure transmitting media (PTM) in separate XRD runs: in the experiment with neon as PTM, XRD was measured between 4.6-11.4 GPa, whereas in the experiment with argon as PTM XRD measurements were performed within the 2.5-30 GPa pressure range. Ruby luminescence (XRD with neon PTM)[31], the equation of state (EoS) of gold (XRD with argon PTM)[32,33], as well as the neon EoS[34,35] and the argon EoS[36,37] in the respective XRD experiments were used for pressure calibration. The Birch-Murnaghan equation of state (B-M EoS)[38,39] was fitted to the pressure-volume P-V data of each Cu_2ZnSnS_4 phase.

B. Computational details

The periodic density functional theory (DFT) calculations were performed with the Vienna Ab initio Simulation Package (VASP) 5.3.5[40–43] at the athermal limit. A plane wave basis set with an energy cutoff of 550 eV was used, in order for the total energy to converge to the sub-milli-Hartree regime. We used projector-augmented wave (PAW) potentials[44,45], whereby the 4s and 3d electrons of Cu and Zn, the 5s, 5p, and 4d electrons of Sn, and the 3s and 3p electrons of S were explicitly considered. The electronic convergence criteria was set at least to 10^{-5} eV, whereby the Blocked-Davidson algorithm was applied as implemented in VASP. The structural relaxation of internal and external lattice parameters was set to a force convergence of $4 \cdot 10^{-2}$ eV/Å^2, performed with the conjugate-gradient algorithm implemented in VASP[46]. The freedom of spin polarization was enabled and a Gaussian smearing approach with a smearing factor σ of 0.01 eV was utilized. For all structures we simulated 16 atoms, which corresponds to the number of atoms in the kesterite unit cell (Fig. S3 in the **Supplement**). For the GeSb-type and RS-type structures we created 1×1×12 supercells to match the number of atoms of the other structure models. The cells

TABLE I: Overview of the reported high-pressure phases of Cu_2ZnSnS_4. PTM stands for the pressure transmitting medium used in each experiment. Literature results are from †: Ref. 24, ‡: Ref. 22. Data presented here are shown in red color.

Cu_2ZnSnS_4 phase	Method	PTM	Pressure stability range ΔP (GPa)
Kesterite-type (KS, SG $I\bar{4}$, $Z = 2$)	Raman and XRD†	Argon	<7-9 GPa
Disordered kesterite-type (DKS, SG $I\bar{4}2m$, $Z = 2$)	Raman and XRD†	Argon	7-9 GPa<P <15 GPa
Disordered rocksalt-type (RS, SG $Fm\bar{3}m$, $Z = 4$)	Raman and XRD†	Argon	>15 GPa
Stannite-type (ST, SG $I\bar{4}2m$, $Z = 2$)	DFT-PBE‡	-	>32 GPa
Kesterite-type (KS, SG $I\bar{4}$, $Z = 2$)	XRD	Argon and Neon	<14-16 GPa
Disordered GeSb-type (SG $I4/mmm$, $Z = 2$)	XRD	Argon	>14-16 GPa
	DFT-PBE	-	16
Disordered zincblende-type (ZB, SG $F\bar{4}3m$, $Z = 4$)	XRD	Argon	Full pressure release

were fully optimized with a 8×8×4 k-grid constructed via the Monkhorst-Pack scheme[47] and centered at the Γ-point with the Perdew, Burke, and Ernzerhof (PBE) functional[48]. The DKS Cu_2ZnSnS_4 phase was treated in the same manner as stated before[17]. On top of the PBE-optimized structures, single point calculations for the band gap E_g and the electronic density of state (DOS) with the Heyd-Scuseria-Ernzerhof HSE06-functional[49–52] were performed with a 4×4×2 k-grid to account for an accurate electronic structure (Fig. S4 in **Supplement**). For systems with a finite band gap, the tetrahedron method with Blöchl corrections[53] was applied for the band structure evaluation.

The pressure dependence was determined by selecting volume points in a range of about ±100 Å^3 around the minima. This corresponds to a pressure range of 0-100 GPa. We used a step size of 8 Å^3 which led to 23 (KS and DKS) and 24 (GeSb-type) volume points, respectively. At each volume point, we optimized the cell shape and the atomic positions. We fitted the B-M EoS function[38,39] to the total energy as a function of volume for each Cu_2ZnSnS_4 phase. Then the pressure of each volume was obtained from the $P(V)$ formulation of the same B-M EoS (Fig. S5 in **Supplement**).

III. RESULTS AND DISCUSSION

A. Structural compression of Cu_2ZnSnS_4 up to 14 GPa: KS→DKS transition?

A former investigation showed that KS-type Cu_2ZnSnS_4 undergoes a structural transition into a DKS modification between 7-9 GPa[24]. This transformation was evidenced by a kink in the pressure-induced evolution of the c-axis between 7-9 GPa, whereas the a-axis became almost incompressible after the transition. In order to verify the aforementioned transition, we performed two separate high-pressure XRD experiments with neon and argon serving as PTM up to ∼11 GPa and ∼14 GPa, respectively.

In Fig. 2 we show selected XRD patterns collected with Ne as PTM, as well as the pressure-induced evolution of the Cu_2ZnSnS_4 tetragonal a and c lattice parameters from all the different high-pressure XRD experiments. Before proceeding further, we should note the following: (a) the Cu_2ZnSnS_4 sample contains a small fraction of Cu_2S impurity (SG $P2_1/c$, $Z = 48$)[54,55], estimated close

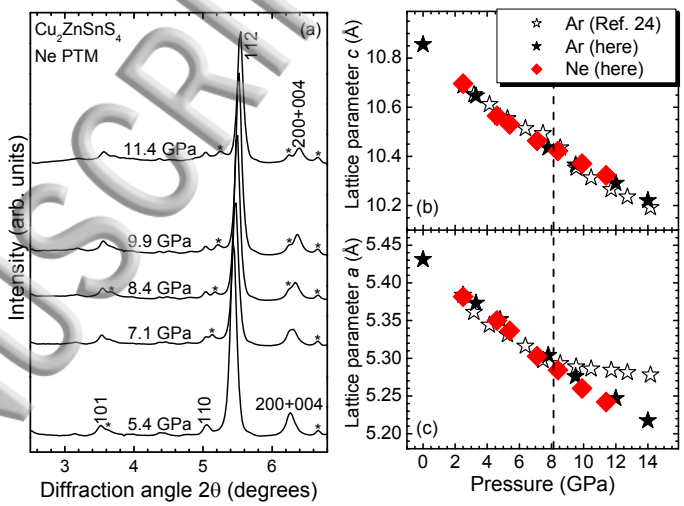

FIG. 2: (a) Enhanced view of the Cu_2ZnSnS_4 XRD patterns within the 2.5-6.5° 2θ diffraction angle range, collected with Ne as PTM ($\lambda = 0.2910$ Å). Background has been subtracted with the help of Chebyshev polynomial functions. The $I\bar{4}$ Miller indices for specific KS Bragg peaks are shown. Asterisks mark the strongest Cu_2S impurity Bragg peaks (see text). (b) Plot of the Cu_2ZnSnS_4 a and c axes as a function of pressure for the different high-pressure XRD runs. The vertical dashed line represents the KS→DKS transition pressure reported before[24]. Error bars are smaller than the symbol size.

to ∼3-5% from the relative Bragg peak intensity ratio at ambient conditions[24]; the presence of this Cu_2S impurity phase appears to be a common byproduct of Cu_2ZnSnS_4 synthesis[15]. (b) Cu_2S is known to undergo two structural transitions at 3.2 GPa and 7.4 GPa towards two different monoclinic phases (and one additional structural transition into an unidentified phase at 26 GPa)[56]; the 7.4 GPa Cu_2S transition is also observed in our 7.1 GPa XRD pattern with neon PTM (denoted as asterisks in Fig. 2).

Direct comparison of the pressure-induced evolution of the Cu_2ZnSnS_4 tetragonal lattice parameters reveals that in the present experiments, with either argon or neon serving as PTM, there are no visible anomalies in the lattice parameters. This observation is in contrast to the previous argon PTM XRD data (Fig. 2). A careful comparison of the measured Debye-Scherrer rings between the former and current high-pressure XRD runs with argon PTM reveals that the inconsistency between the XRD experiments arose due to the incorrect

assignment of the Bragg peaks located at 6-6.8° in the previous argon PTM XRD experiment. In particular, the lower argon PTM XRD study recorded two separate Bragg peaks within the 6-6.8° 2θ region, where the 200 and 004 KS Bragg peaks are expected. Consequently, these two Bragg features were assigned to the 200 and 004 KS Bragg peaks. Considering the newer argon and neon PTM XRD experiments presented here, we could conclude that one of these Bragg peaks was actually originating from the 111 Bragg peak of the argon PTM[37]. This misinterpretation of the collected XRD data led to the observed incompressibility of the *a*-crystallographic axis in the first argon XRD experiment, and the basic argument behind the KS→DKS transition in Cu_2ZnSnS_4 (Fig. 2). A direct comparison between the Debye-Scherrer rings and the respective integrated XRD diffractograms of the various XRD experiments at 12 GPa are provided in Fig. S1 and Fig. S2 in the **Supplement**.

Despite the apparent absence of a 'clear' KS→DKS transition in Cu_2ZnSnS_4, a more accurate way to identify subtle anomalies in the structural parameters under pressure is through the plotting of the normalized stress F as a function of the Eulerian strain f_E[57]. Generally, the F-f_E parameters should exhibit a linear relationship, with any divergence from a linear trend hinting potential structural changes[58]. Such deviation was e.g. observed in the earlier report on the KS→DKS transition in Cu_2ZnSnS_4 between 7-9 GPa[24]. The relevant F-f_E plots for the volume V (F_V-f_{EV}), as well as for the tetragonal Cu_2ZnSnS_4 a (F_a-f_{Ea}) and c (F_c-f_{Ec}) lattice parameters obtained from both the argon and neon PTM XRD experiments here are shown in Fig. 3. From these plots, we can immediately observe a break in both the F-f_E plots of the a- and c-axes taking place close to 6 GPa; on the other hand, no effect can be seen in the respective F-f_E volume plots for either PTM XRD run (Fig. 3c). We attribute these F-f_E anomalies close to 6 GPa to a subtle pressure-induced change of the compressibility mechanism/behavior of the KS Cu_2ZnSnS_4 structure.

More information on this pressure-induced structural effects observed in the KS Cu_2ZnSnS_4 structure close to 6 GPa can be obtained from the pressure-induced evolution of the relevant interatomic parameters. In the KS structure, the metal cations are located in special Wyckoff positions, with the Cu(1), Cu(2), Zn, and Sn cations occupying the 2a (0, 0, 0), 2c (0, 0.5, 0.25), 2d (0, 0.5, 0.75), and 2b (0, 0, 0.5) sites, respectively[9,26,60]. On the other hand, the S anion resides in the general Wyckoff position 8g (x, y, z), with the S-x, S-y, and S-z atomic coordinates free to vary upon pressure increase. This variation is depicted in Fig. 4. We can readily observe a change in the pressure-slopes of the S-x and S-y coordinates around 6 GPa, in excellent agreement with the F-f_E anomalies (Fig. 3). This is also reflected in the pressure dependence of the Cu(1)-S interatomic bond length (Fig. 4).

In order to check for a possible pressure-induced KS→DKS transition in Cu_2ZnSnS_4 as the origin behind these anomalies, as speculated earlier[24], we have calculated the respective enthalpy difference between the KS and DKS Cu_2ZnSnS_4 phases by means of DFT. The results are displayed collectively in Fig. 5. As we can observe, the DKS phase *always* lies higher than the KS structure enthalpy-wise for all pressures investigated here. We remind here that the main structural difference between the tetragonal KS and DKS structures is the mixed occupancy between the Cu and Zn sites lying in the z = 1/4 and z = 3/4 cationic layers of DKS, which in turn is manifested as an expansion of the long c-axis[17]. Considering that such change is not supported by the present high-pressure XRD results (Fig. 2), as well as the finite KS and DKS enthalpy difference, we can safely conclude at this stage that the experimentally observed changes in the F-f_E (Fig. 3) and interatomic parameters' pressure-induced evolution (Fig. 4) are most likely not originating from a KS→DKS transition. Hence, which effects can account for these anomalies?

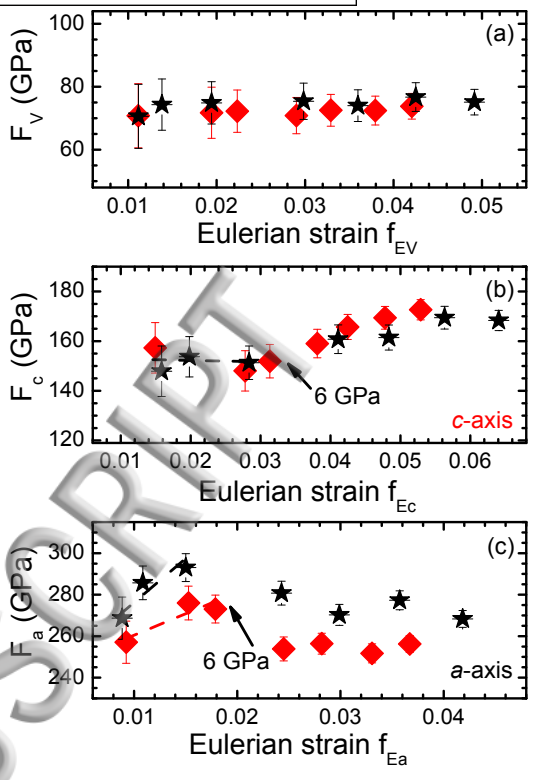

FIG. 3: Plot of the normalized stress F as a function of the Eulerian strain f_E for the (a) volume V, (b) the c- and (c) a-axes for the KS tetragonal Cu_2ZnSnS_4 phase. The argon and neon PTM XRD data are shown in black star and red rhombic symbols, respectively. The F-f_E quantities for the volume are calculated from the structural data (Fig. 2) as follows: $f_{EV} = [(V_0/V)^{2/3}\text{-}1]/2$ and $F_V = P/3f_{EV}(1+2f_{EV})^{5/2}$, where V_0 is the ambient-pressure volume of the KS phase, V is the volume, and P is pressure (in GPa)[57]. For the lattice parameters: $f_{Ea} = [(a_0/a)^2\text{-}1]/2$, $F_a = P(ac_0/a_0c)^{2/3}/f_{Ea}(1+2f_{EV})^{5/2}$ for the a-axis, and $f_{Ec} = [(c_0/c)^2\text{-}1]/2$, $F_c = P(a_0c/ac_0)^{4/3}/f_{Ec}(1+2f_{EV})^{5/2}$ for the c-axis[59].

Before offering any reasoning, we should remind here that in the previous high-pressure Raman spectroscopic measurements on Cu_2ZnSnS_4 conducted with argon PTM, the emergence of a new D band at 335 cm^{-1} was detected at 1.2 GPa already[24], far below the pressure-

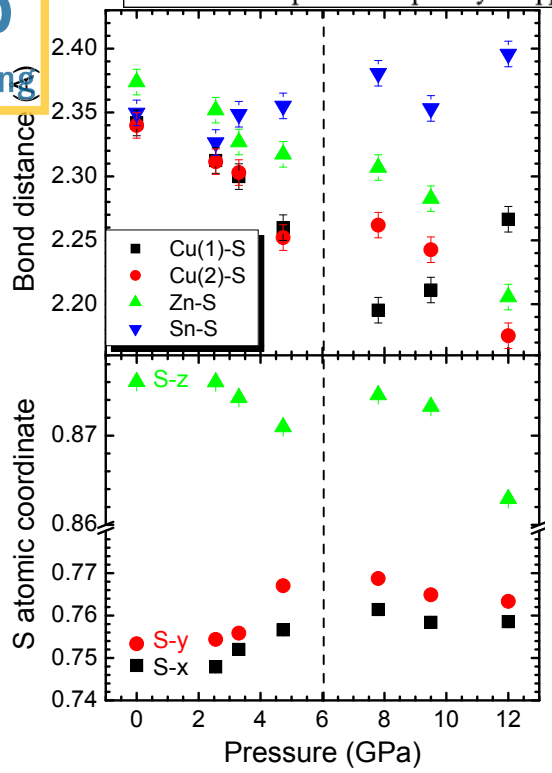

FIG. 4: Plot of the S atomic coordinates (bottom) and selected interatomic bond lengths (top) as a function of pressure for the KS Cu_2ZnSnS_4 phase, as extracted from the XRD measurements. The vertical dashed line depicts the onset of the pressure-induced changes (see text).

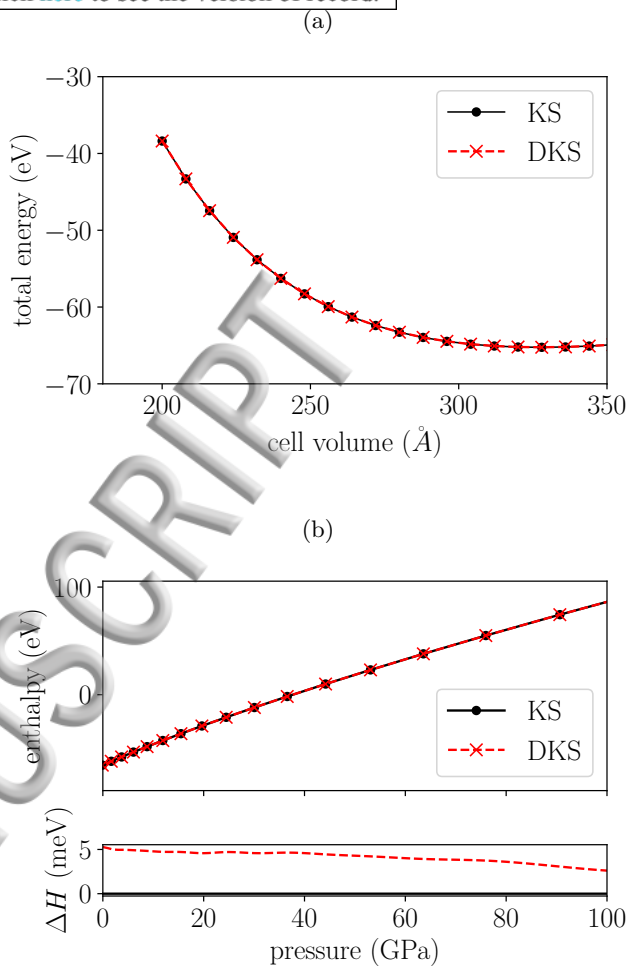

FIG. 5: (a) Volume-energy V-E plot for the KS (black circles) and DKS (red crosses) phases. (b) The calculated enthalpies of the KS and DKS phases as a function of pressure, as well as the respective KS and DKS enthalpy difference ΔH with respect to pressure. Enthalpy H is defined as $H(P) = E + PV$, and a phase is stable if it has a lower value of H.

related subtle structural effects observed here (Fig. 3 and Fig. 4). This D band lied ∼3 cm^{-1} lower in terms of Raman frequency shift compared to the most intense A band of the KS phase at 338 cm^{-1} (zero-pressure value); the latter is assigned to the sulfur S-S stretching vibrations along the KS c-axis (the metal cations are not involved in this vibration)[61,62]. Upon pressure increase, this D Raman feature becomes dominant intensity-wise at the expense of the KS A mode in the Cu_2ZnSnS_4 Raman spectra close to 9 GPa, whereas their ∼3 cm^{-1} frequency difference persisted throughout the investigated pressure range[24].

This D band has been commonly associated with the well-documented Cu-Zn anti-site cationic exchange in KS Cu_2ZnSnS_4[11,20,63], the presence of a stannite Cu_2ZnSnS_4 component[64], or arising due to phonon confinement effects[65]. Among these possibilities, we can probably exclude the phonon confinement scenario due to the μm grain size of the investigated Cu_2ZnSnS_4 polycrystalline samples, as this model applies in nanocrystalline materials[65]. Moreover, the presence of a ST Cu_2ZnSnS_4 modification under these pressure conditions can be also excluded according to our DFT-PBE enthalpy calculations (Fig. S6 in the **Supplement**). As for the Cu-Zn anti-site exchange possibility, given our aforementioned discussion, we can most likely exclude this scenario as well. The intensity-wise dominance of the D Raman band compared to the KS A mode above 9 GPa implies the existence of an almost fully (or at least partially) disordered Cu_2ZnSnS_4 phase, leading in turn to the adoption of a DKS phase. Such type of disorder, however, should be also captured in the interatomic bond lengths to some extent, since (a) the Cu-S and Zn-S bond distances are distinctly different in terms of values, and (b) a pressure-induced averaging of these bond lengths due to the Cu-Zn anti-site exchange should yield characteristic changes in the respective interatomic bond distances[17]; this picture cannot be verified unambiguously in our case, mainly due to the absence of any visible Zn-S bond-related anomalies (Fig. 4). Our XRD data clearly show that the anomalies are mainly related to the Cu(1)-S bond (Fig. 4). Regarding other well-documented intrinsic defect complexes in Cu_2ZnSnS_4, none is limited to the Cu(1) sites[15,66]. Hence, we tend to exclude any type of pressure-induced cationic disorder or vacancy formation triggering either the presence and intensity enhancement of the Raman D band, or the F-f_E and Cu-S anomalies in KS Cu_2ZnSnS_4 (Fig. 3 and Fig. 4).

Regarding the former, we should remind here that B and E symmetry Raman-active modes may be present in the vicinity of the 338 cm^{-1} KS A mode[61–64]. The exact positions of these Raman-active vibrations may vary depending on the Cu_2ZnSnS_4 sample preparation method[61–64]. Hence, a simple explanation behind the presence of the Raman D band (even at low pressures) might be that it actually corresponds to a different B/E KS vibration, which becomes detectable in the Cu_2ZnSnS_4 Raman spectra upon moderate compression. The pressure-induced intensity enhancement of the D band on the other hand[24], may be connected with an increasing electronic polarizability of this mode compared to its adjacent A KS Raman peak under compression.

Another scenario accounting for both the observed F-f_E and Cu-S anomalies, as well as the intensity enhancement of the Raman D band, might be that all of these effects reflect pressure-induced electronic changes in Cu_2ZnSnS_4, e.g. a topological transition of the Cu-related electronic DOS under moderate compression. Such pressure-induced electronic topological transitions constitute a common motif for layered materials, and are evidenced by distinct compressibility and Raman intensity changes, without any alteration of the (average) crystalline symmetry[58,67–69]. A thorough investigation of such possibility, however, lies beyond the scope of the present paper.

B. Structural compression of Cu_2ZnSnS_4 up to 30 GPa with argon PTM

We turn now to the Cu_2ZnSnS_4 structural transition reported close to 15 GPa towards a disordered RS-type modification (Table I), where all of the metal cations exhibit random/mixed occupancy of the cationic site[24]. The previous investigation was conducted up to ~18 GPa, with argon serving as PTM; here we have expanded upon the previous high-pressure studies up to 30 GPa, again with argon as PTM for consistency.

The results are presented in Fig. 6. We can observe that the KS phase persists up to ~14 GPa; at this pressure, several new Bragg peaks appear in the XRD patterns, signifying a structural transition. The transition is completed at 15.8 GPa, in excellent agreement with the earlier result[24]. Analysis of the measured XRD patterns reveals that the RS-type phase could reproduce the XRD diffractogram measured at 15.8 GPa; the following XRD pattern collected at 18.5 GPa, however, could not be fitted with the cubic RS-type structure satisfactorily. This prompted us to use a tetragonally-distorted RS-type modification, noted here as GeSb-type (SG $I4/mmm$, $Z = 2$)[70], which resulted in a significantly improved XRD refinement (Fig. 6). We should point out here that the reason behind this unsuccessful RS-type structure indexing attempt involves the pressure-induced evolution of the recorded Bragg peak positions, which do not follow the cubic RS-type structural trend (for more details, see Fig. S7 in **Supplement**).

Therefore, Cu_2ZnSnS_4 is apparently adopting another disordered GeSb-type structure above ~18 GPa, again with a mixed/random occupancy of the cationic site by

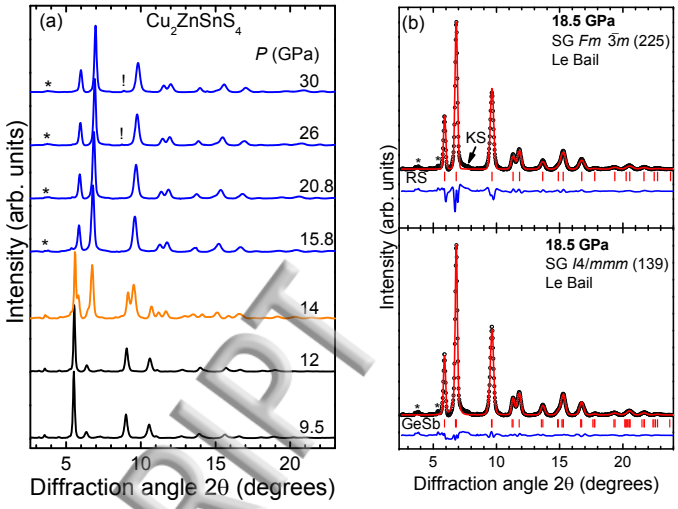

FIG. 6: (a) Selected XRD patterns of Cu_2ZnSnS_4 at various pressures with Ar PTM ($\lambda = 0.2913$ Å). The black, orange, and blue patterns indicate the KS, KS/GeSb coexistence, and GeSb-type phases, respectively (see text). Background has been subtracted for clarity with Chebyshev polynomial functions. Asterisks and exclamation marks indicate the strongest Bragg peaks of the Cu_2S impurity phase and the argon PTM[36,37], respectively. (b) Examples of Le Bail refinements at 18.5 GPa, using both the RS-type (top) and the tetragonally distorted GeSb-type (bottom) modifications. The black circles and the red solid curves correspond to the measured and the calculated patterns, whereas their difference is depicted as blue curves. The starting structural parameters are taken from Ref. 24 (RS-type) and Ref. 70 (GeSb-type). The arrow indicates KS phase residue, and asterisks mark the strongest Bragg peaks of the Cu_2S impurity.

the Cu/Zn/Sn ions. This phase persists up to 30 GPa, the highest pressure reached here. A reasonable question which arises, however, is the following: does Cu_2ZnSnS_4 adopt the RS-type modification within a limited pressure range, i.e. between 15-18 GPa, or is the GeSb-type phase adopted from 15 GPa already? Considering the relevant theoretical results at our disposal, we tend to favor the second scenario. We will return to this point later below.

In Fig. 7 we plot the extracted structural parameters for the various phases of Cu_2ZnSnS_4 obtained with argon PTM (this run alone). As we can observe, the KS→GeSb-type structural transition is accompanied by a ~15% volume change at the transition point. The latter volume drop results from the increase in the cationic coordination with respect to the S^{2-} anions from four to six (Fig. 1). The B-M EoS fitting results of the P-V data are listed in Table II.

In order to acquire certain insights on the aforementioned pressure-induced KS→GeSb-type structural transition in Cu_2ZnSnS_4, we have calculated the enthalpies ($H(P) = E + PV$) for the starting KS phase and the disordered GeSb-type modification (Fig. 8). Additionally, we have calculated the enthalpies of several reported Cu_2ZnSnS_4 polymorphs, such as a modified wurtzite-type phase (WZ, SG $P2_1$), the aforementioned DKS modification (SG $P\bar{4}$), the stannite-type structure (ST, SG $I\bar{4}2m$), and the primitive mixed Cu-Au phase

TABLE II: Volume per formula unit V/f.u., bulk modulus B, and the bulk modulus pressure derivative B' for the various phases of Cu_2ZnSnS_4 at the respective reference pressure P, as obtained by Birch-Murnaghan EoS functions[38,39] fitted to our measured and computed P-V data. The term 'Fixed' means that the corresponding parameters were not allowed to vary during the EoS fitting. Other results are from ⋆: Ref. 61, ‡: Ref. 22 (N/A: not available).

Cu_2ZnSnS_4 phase	Method	P (GPa)	V/f.u. (Å^3)	B (GPa)	B' (GPa)
$I\bar{4}$ (KS)	EXP	0.0	160.1 (fixed)	74(2)	4.4(4)
	GGA-PBE	0.0	163.75	68.64	4.64
	LDA⋆	0.0	150.7	89.4	N/A
	GGA‡	0.0	164.61	63.94	N/A
$I4/mmm$ (GeSb-type)	EXP	15.8	119.4 (fixed)	213(4)	4.0 (fixed)
	GGA-PBE	16	120.75	298.53	2.03

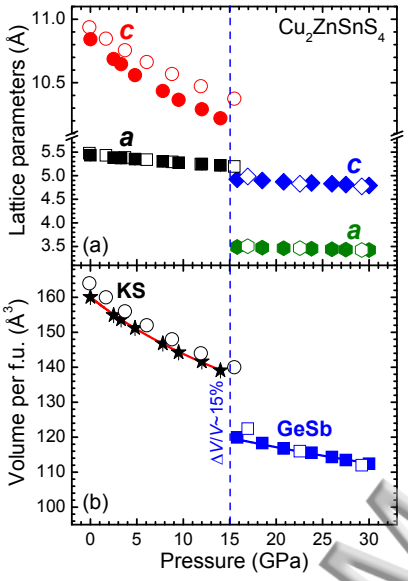

FIG. 7: Pressure-induced variation of the (a) lattice parameters and (b) volume per formula unit (f. u.) for the various phases of Cu_2ZnSnS_4 with argon serving as PTM. The solid curves through the P-V data correspond to fitted B-M EoS functions[38,39]. The closed and open symbols correspond to experimental and DFT-PBE calculated data, respectively. The vertical dashed lines depict the onset of the KS→GeSb-type structural transition. Error bars are smaller than the symbols.

(PMCA, SG $P\bar{4}2m$) (Fig. S6 in **Supplement**). As we can observe from the relative enthalpy difference between the KS and the GeSb-type phases, the transition is predicted to take place at 16 GPa, in excellent agreement with the experimental transition pressure value between 14-16 GPa (Fig. 7). The respective lattice parameters and volumes for the KS and GeSb-type Cu_2ZnSnS_4 structures are plotted alongside their experimental counterparts in Fig. 7. Generally we can observe a very good agreement, with the exception of the KS c-axis, which is overestimated within the DFT-PBE approximation[71]. We note that in our calculations performed up to 100 GPa we could not observe a transition from the KS phase towards a stannite structure, or any of the other examined phases (Fig. S6 in **Supplement**), in contrast to *Zhao et al.*[22]. The respective calculated volumes, bulk moduli, and bulk moduli derivatives for the KS and GeSb-type phases at the respective reference pressures P are listed in Table II.

Finally, upon full decompression, the GeSb-type structure transforms into a disordered sphalerite-type (ZB-type) phase (Fig. 1 and Fig. S8 in **Supplement**). This back-transformation indicates that even though the pressure-induced cationic coordination increase from four to six is reversible in Cu_2ZnSnS_4, the cationic disordering of the structure, i.e. the random occupation of the various Wyckoff sites by the Cu, Zn, and Sn constituent metals can be quenched back to ambient pressure. This aspect of metastable structural disorder upon decompression appears to be a common trend among the relevant ternary chalcopyrite-type compounds[72–76]. The adoption of a disordered ZB-type structure upon decompression is also consistent with the relevant Raman spectra collected upon decompression in the earlier high-pressure Raman study conducted with argon PTM[24]. In particular, the Raman response of the recovered Cu_2ZnSnS_4 phase indicated strong signs of structural disorder, i.e. broad Raman features, whereas the Raman spectrum was reminiscent of the starting tetrahedrally-coordinated KS phase, with two broad Raman bands located at ~ 270 cm^{-1} and at 330 cm^{-1} (the KS Raman spectrum is characterized by two intense Raman peaks at ~ 291 cm^{-1} and at 338 cm^{-1} at ambient conditions, see Fig. 2 in Ref. 24. This frequency downshift of the most significant Raman features in the ZB-type phase compared to the KS structure can be related to the cationic disorder present in the former phase. All in all, these Raman-related observations are fully agreeing with the current XRD results.

C. Electronic properties of Cu_2ZnSnS_4 under pressure

We turn now to the calculated electronic DOS for the KS and GeSb-type Cu_2ZnSnS_4 structures (Fig. 9). As we can observe, the KS band structure below the Fermi level E_F is mainly dominated by the occupied Cu 3d and S 2p states, whereas the unoccupied S 3p and Sn 5p levels contribute mainly to the DOS above E_F. The calculated band gap E_g of the KS phase is 1.18 eV at ambient pressure, in very good agreement with previous calculations[23,77,78] and experimental results[1,79,80]. The KS E_g increases upon compression and reaches a value close to 2 eV at the KS→GeSb-type (calculated) structural transition pressure of 16 GPa; this pressure-induced E_g shift is consistent with previous works[23,81].

Upon adopting the GeSb-type phase, the Cu_2ZnSnS_4

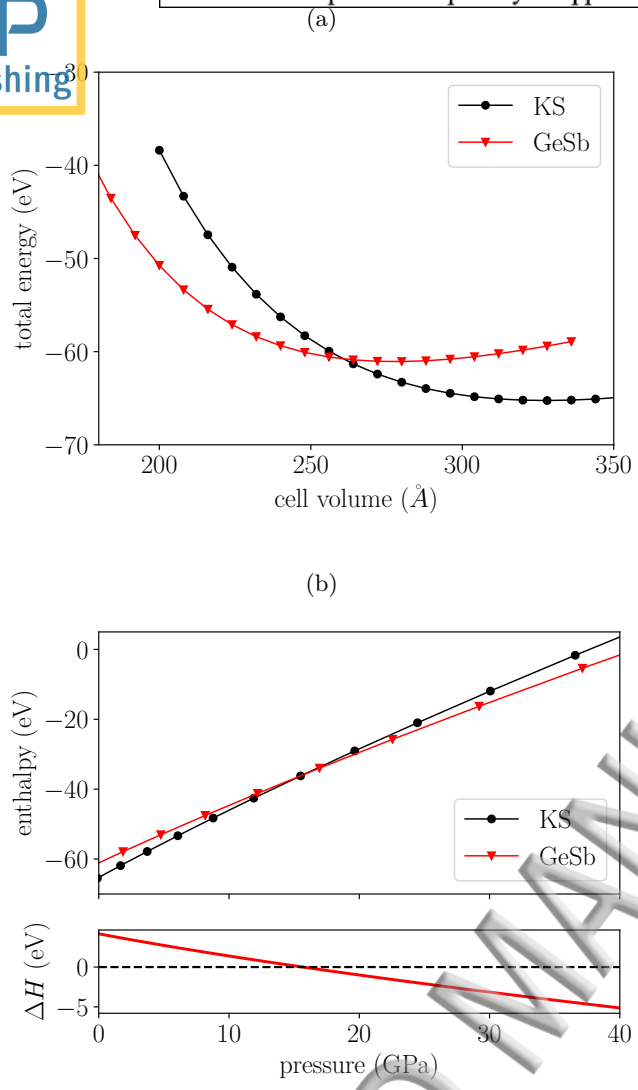

FIG. 8: (a) Volume-energy V-E plot for the KS (black circles) and GeSb-type (red triangles) phases. (b) Top panel: The calculated enthalpies of the KS and GeSb-type phases as a function of pressure. Bottom panel: The enthalpy difference between the KS and GeSb-type phases with respect to pressure. The enthalpy H is defined as $H(P) = E + PV$, and a phase is stable if it has a lower value of H.

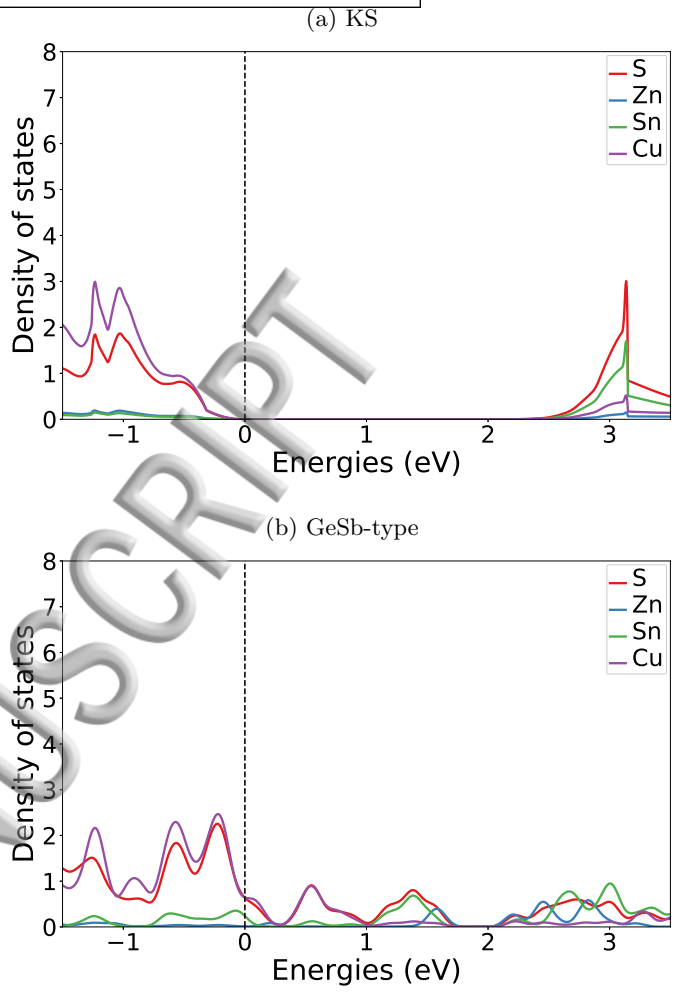

FIG. 9: DFT-HSE06 calculated density of states (DOS) for the Cu_2ZnSnS_4 (a) KS and (b) GeSb-type phases, both at the transition pressure of 16 GPa. The Fermi level E_F is set at zero.

DOS changes drastically. In particular, the calculated electronic band structure reveals the presence of electronic states around E_F, thus indicating that the GeSb-type modification of Cu_2ZnSnS_4 shows metallic conductivity (Fig. 9). Given that pressure-induced structural transitions of binary and ternary compounds, which involve cationic coordination increase from fourfold to sixfold, tend to exhibit concomitant insulator-to-metal transitions[82], our finding is in line with the established pressure-induced structural and electronic trends.

D. Discussion

The disordered GeSb-type high-pressure modification of Cu_2ZnSnS_4 was shown to better index the experimental XRD diffractograms above 18 GPa, compared to the previously assigned disordered RS-type structure adopted at ∼15 GPa[24] (Fig. 6 and Fig. S7 in the **Supplement**). Since the Le Bail refinements of the XRD patterns with either the RS-type or the GeSb-type structural models yield identical results within the 15-18 GPa pressure range, a clear conclusion over the exact pressure-induced structural path of Cu_2ZnSnS_4 cannot be drawn. For this reason, we turn to our DFT-PBE results. In Fig. 10 we plot the calculated enthalpy difference of the RS-type and GeSb-type Cu_2ZnSnS_4 modifications as a function of pressure. We can observe that the RS-type structure lies *always* higher than the GeSb-type one in terms of enthalpy for all the investigated pressures. Hence, our DFT-PBE results favor the existence of the GeSb-type phase as the high-pressure modification of Cu_2ZnSnS_4. Considering also that the high-pressure Raman spectra reported earlier do not show any appreciable

This manuscript was accepted by J. Appl. Phys. Click here to see the version of record.

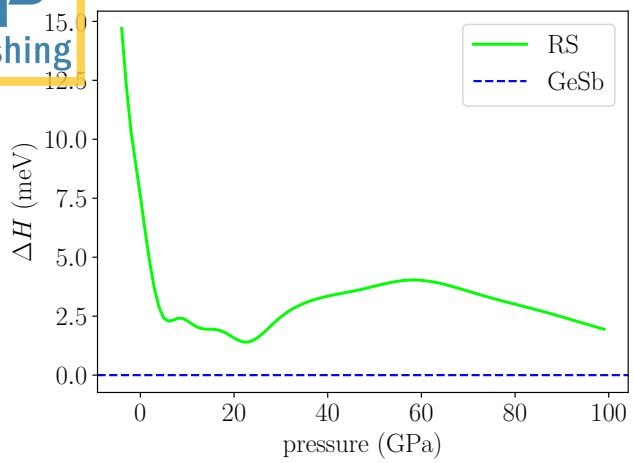

FIG. 10: Enthalpy difference between the RS-type and GeSb-type Cu_2ZnSnS_4 polymorphs with respect to pressure at 0 K.

changes within the 15-18 GPa pressure range[24], we conclude that the disordered tetragonal GeSb-type phase is the proper choice for describing the high-pressure structure of Cu_2ZnSnS_4 modification above 16 GPa (Fig. 6).

Since the KS phase is structurally related to the chalcopyrite structure, a comparison between the high-pressure behavior of these relevant chalcopyrite-type systems with Cu_2ZnSnS_4 is in order. Regarding the former, both the ternary chalcopyrite-type ABX_2 (SG $I\bar{4}2d$) and defect chalcopyrite AB_2X_4 (SG $I\bar{4}$) compounds exhibit similar structural and electronic trends. In particular, structural transitions from the starting tetragonal phases towards disordered RS-type structures have been reported for several chalcopyrite-based materials of varying chemical compositions[72–76,83–87]. All of these transitions are accompanied by electronic changes towards metallic states. Another interesting structural aspect is the fact that decompression does not lead to the recovery of either the starting chalcopyrite-type or the high-pressure RS-type modifications in these materials, but rather towards disordered ZB-type phases[72–76].

Within this framework, the reported high-pressure behavior of KS Cu_2ZnSnS_4 (i.e. the KS→disordered GeSb-type transition, and the adoption of a disordered ZB-type modification upon decompression) is in agreement with the generic high-pressure structural and electronic trends of the structurally-related chalcopyrite-type compounds.

IV. CONCLUSIONS

We have investigated the high-pressure structural and electronic properties of kesterite-type Cu_2ZnSnS_4, with a combination of XRD and first-principles methods. Our investigations indicate that the previously reported kesterite→disordered kesterite structural transition between 7-9 GPa[24] originated from the misinterpretation of specific XRD features. Nevertheless, subtle pressure-induced changes of the compressibility mechanism/behavior are indeed taking place in kesterite-type Cu_2ZnSnS_4 close to 6 GPa, as evidenced by distinct anomalies in the F-f_E plots and in the pressure-induced evolution of the Cu(1)-S bond length, but without any change of the average crystalline symmetry; the exact origin of these subtle changes is unclear at this stage.

Further pressure increase to 16 GPa led to a transition towards a disordered GeSb-type polymorph with tetragonal symmetry. The cationic coordination increases from four to six upon the kesterite→disordered GeSb-type transition. Our DFT-PBE calculations reproduced the experimental observations accurately, as (a) no sign of kesterite→disordered kesterite transition was found, and (b) the kesterite→disordered GeSb-type transition was calculated to take place at 16 GPa. In addition, band structure calculations revealed that the kesterite→disordered GeSb-type structural transition is accompanied by a semiconductor-to-metal transition, in agreement with the available results on structurally similar materials[73,82]. Finally, full decompression resulted in the adoption of a disordered sphalerite/zincblende structure, where the tetrahedrally-coordinated cations retain mixed/random occupancies.

ACKNOWLEDGMENTS

Parts of this research were carried out at the light source PETRA III (DESY), a member of the Helmholtz Association (HGF). The North-German Supercomputing Alliance (HLRN) and computer facilities of the Freie Universität Berlin (ZEDAT) are acknowledged for computer time. Financial support from the MatSEC graduate school of the Helmholtz Zentrum Berlin (HZB) in cooperation with the Dahlem Research School (A. R. and M. Q.) and the International Max Planck Research School (IMPRS) is gratefully acknowledged.

[1] H. Katagiri, K. Jimbo, W. S. Maw, K. Oishi, M. Yamazaki, H. Araki, and A. Takeuchi, Thin Solid Films **517**, 2455 (2009).
[2] X. Liu, Y. Feng, H. Cui, F. Liu, X. Hao, G. Conibeer, D. B. Mitzi, and M. Green, Progress in Photovoltaics: Research and Applications **24**, 879 (2016).
[3] S. Chen, X. G. Gong, A. Walsh, and S.-H. Wei, Applied Physics Letters **94**, 041903 (2009), http://dx.doi.org/10.1063/1.3074499.
[4] J. J. Scragg, P. J. Dale, L. M. Peter, G. Zoppi, and I. Forbes, Phys. stat. sol. (b) **245**, 1772 (2008).
[5] S. Siebentritt and S. Schorr, Progr. Photovoltaics **20**, 512 (2012).
[6] K. Sun, C. Yan, F. Liu, J. Huang, F. Zhou, J. A. Stride, M. Green, and X. Hao, Advanced Energy Materials **6**, 1600046 (2016), 1600046.
[7] W. Shockley and H. J. Queisser, J. Appl. Phys. **32**, 510 (1961).
[8] L. Choubrac, M. Paris, A. Lafond, C. Guillot-Deudon, X. Rocquefelte, and S. Jobic, Phys. Chem. Chem. Phys. **15**, 10722 (2013).
[9] S. Schorr, Sol. Energy Mater. Sol. Cells **95**, 1482 (2011).
[10] S. Schorr, Thin Solid Films **515**, 5985 (2007).
[11] R. Caballero, E. Garcia-Llamas, J. M. Merino, M. Leon, I. Babichuk, V. Dzhagan, V. Strelchuk, and M. Valakh, Acta Mater. **65**, 412 (2014).
[12] S. Chen, X. G. Gong, A. Walsh, and S.-H. Wei, Appl. Phys. Lett. **96**, 021902 (2010).
[13] S. Chen, J.-H. Yang, X. G. Gong, A. Walsh, and S.-H. Wei, Phys. Rev. B **81**, 245204 (2010).
[14] M. Paris, L. Choubrac, A. Lafond, C. Guillot-Deudon, and S. Jobic, Inorganic Chemistry **53**, 8646 (2014), http://dx.doi.org/10.1021/ic5012346.

[15] L. E. V. Rios, K. Neldner, G. Gurieva, and S. Schorr, Journal of Alloys and Compounds **657**, 408 (2016).
[16] M. Grossberg, J. Krustok, J. Raudoja, and T. Raadik, Appl. Phys. Lett. **101**, 102102 (2012).
[17] M. Quennet, A. Ritscher, M. Lerch, and B. Paulus, Journal of Solid State Chemistry **250**, 140 (2017).
[18] S. Schorr and G. Gonzalez-Aviles, Phys. Stat. Sol. (a) **206**, 1054 (2009).
[19] J. J. S. Scragg, L. Choubrac, A. Lafond, T. Ericson, and C. Platzer-Bjorkman, Appl. Phys. Lett. **104**, 041911 (2014).
[20] M. Y. Valakh, V. M. Dzhagan, I. S. Babichuk, X. Fontane, A. Perez-Rodriquez, and S. Schorr, JETP Letters **98**, 255 (2013).
[21] Y. Zhao, D. Li, and Z. Liu, Mod. Phys. Lett. B **30**, 1650176 (2016).
[22] Y. Zhao, D. Li, and Z. Liu, J. Alloys Comp. **696**, 86 (2017).
[23] Y. Zhao, D. Li, and Z. Liu, Journal of Electronic Materials **46**, 2812 (2017).
[24] I. Efthimiopoulos, A. Ritscher, M. Lerch, S. Speziale, A. S. Pakhomova, H. P. Liermann, and M. Koch-Müller, Applied Physics Letters **110**, 041905 (2017).
[25] A. Ritscher, A. Franz, S. Schorr, and M. Lerch, J. Alloys Comp. **689**, 271 (2016).
[26] A. Ritscher, M. Hoelzel, and M. Lerch, J. Sol. St. Chem. **238**, 68 (2016).
[27] A. Ritscher, J. Just, O. Dolotko, S. Schorr, and M. Lerch, J. Alloys Comp. **670**, 289 (2016).
[28] H.-P. Liermann, Z. Konopkova, W. Morgenroth, K. Glazyrin, J. Bednarcik, E. E. McBride, S. Petitgirard, J. T. Delitz, M. Wendt, Y. Bican, A. Ehnes, I. Schwark, A. Rothkirch, M. Tischer, J. Heuer, H. Schulte-Schrepping, T. Kracht, and H. Franz, J. Synchrotron Rad. **22**, 908 (2015).
[29] A. P. Hammersley, S. O. Svensson, M. Hanfland, A. N. Fitch, and D. Hausermann, High Pres. Res. **14**, 235 (1996).
[30] B. H. Toby, J. Appl. Crystallogr. **34**, 210 (2001).
[31] K. Syassen, High Press. Res. **28**, 75 (2008).
[32] S.-H. Shim, T. S. Duffy, and T. Kenichi, Earth Planet. Sci. Lett. **203**, 729 (2002).
[33] K. Takemura and A. Dewaele, Phys. Rev. B **78**, 104119 (2008).
[34] A. Dewaele, F. Datchi, P. Loubeyre, and M. Mezouar, Phys. Rev. B **77**, 094106 (2008).
[35] R. J. Hemley, C. S. Zha, A. P. Jephcoat, H. K. Mao, L. W. Finger, and D. E. Cox, Phys. Rev. B **39**, 11820 (1989).
[36] D. Errandonea, R. Boehler, S. Japel, M. Mezouar, and L. R. Benedetti, Phys. Rev. B **73**, 092106 (2006).
[37] M. Ross, H. K. Mao, P. M. Bell, and J. A. Xu, J. Chem. Phys. **85**, 1028 (1986).
[38] F. Birch, Physical Review **71**, 809 (1947).
[39] F. Birch, J. Geophys. Res. **83**, 1257 (1978).
[40] G. Kresse and J. Furthmüller, Computational Materials Science **6**, 15 (1996).
[41] G. Kresse and J. Furthmüller, Physical Review B **54**, 11169 (1996).
[42] G. Kresse and J. Hafner, Physical Review B **47**, 558 (1993).
[43] G. Kresse and J. Hafner, Physical Review B **49**, 14251 (1994).
[44] P. E. Blöchl, Physical Review B **50**, 17953 (1994).
[45] G. Kresse and D. Joubert, Physical Review B **59**, 1758 (1999).
[46] E. Ziegel, W. Press, B. Flannery, S. Teukolsky, and W. Vetterling, Technometrics **29**, 501 (1987).
[47] H. J. Monkhorst and J. D. Pack, Physical Review B **13**, 5188 (1976).
[48] J. P. Perdew, K. Burke, and M. Ernzerhof, Phys. Rev. Lett. **77**, 3865 (1996).
[49] J. Heyd and G. E. Scuseria, The Journal of Chemical Physics **121**, 1187 (2004).
[50] J. Heyd, G. E. Scuseria, and M. Ernzerhof, Journal of Chemical Physics **118**, 8207 (2003).
[51] J. Heyd, G. E. Scuseria, and M. Ernzerhof, The Journal of Chemical Physics **124**, 219906 (2006).
[52] A. V. Krukau, O. A. Vydrov, A. F. Izmaylov, and G. E. Scuseria, The Journal of Chemical Physics **125**, 224106 (2006).
[53] P. E. Blöchl, O. Jepsen, and O. K. Andersen, Physical Review B **49**, 16223 (1994).
[54] H. T. E. Jr., Amer. Miner. **66**, 807 (1981).
[55] H. T. E. Jr., Nature **232**, 69 (1971).
[56] D. Santamaria-Perez, G. Garbarino, R. Chulia-Jordan, M. A. Dobrowolski, C. Muehle, and M. Jansen, J. Alloys Comp. **610**, 645 (2014).
[57] R. J. Angel, Rev. Miner. Geochem. **41**, 35 (2000).
[58] A. Polian, M. Gauthier, S. M. Souza, D. M. Triches, J. C. de Lima, and T. A. Grandi, Phys. Rev. B **83**, 113106 (2011).
[59] C. Meade and R. Jeanloz, Geophys. Res. Lett. **17**, 1157 (1990).
[60] S. Schorr, H. J. Hoebler, and M. Tovar, Eur. J. Miner. **19**, 65 (2007).
[61] T. Gurel, C. Sevik, and T. Cagin, Phys. Rev. B **84**, 205201 (2011).
[62] J. M. Skelton, A. J. Jackson, M. Dimitrievska, S. K. Wallace, and A. Walsh, APL Mater. **3**, 041102 (2015).
[63] X. Fontane, V. Izquierdo-Roca, E. Saucedo, S. Schorr, V. Yukhymchuk, M. Y. Valakh, A. Perez-Rodriguez, and J. R. Morante, J. Alloys Comp. **539**, 190 (2012).
[64] A. Khare, B. Himmetoglu, M. Johnson, D. J. Norris, M. Cococcioni, and E. S. Aydil, Journal of Applied Physics **111** (2012), 10.1063/1.4704191.
[65] M. Dimitrievska, A. Fairbrother, A.Perez-Rodriguez, E. Saucedo, and V. Izquierdo-Roca, Acta Mater. **70**, 272 (2014).
[66] C. J. Bosson, M. T. Birch, D. P. Halliday, C. C. Tang, A. K. Kleppe, and P. D. Hatton, Chem. Mater. **29**, 9829 (2017).
[67] I. Efthimiopoulos, J. Kemichick, X. Zhou, S. V. Khare, D. Ikuta, and Y. Wang, J. Phys. Chem. A **118**, 1713 (2014).
[68] R. Juneja, R. Shinde, and A. K. Singh, J. Phys. Chem. Lett. **9**, 2202 (2018).
[69] A. Ohmura, Y. Higuchi, T. Ochiai, M. Kanou, F. Ishikawa, S. Nakano, A. Nakayama, Y. Yamada, and T. Sasagawa, Phys. Rev. B **95**, 125203 (2017).
[70] B. C. Giessen and C. Borromee-Gautier, J. Sol. St. Chem. **4**, 447 (1972).
[71] S. Baroni, S. de Gironcoli, A. D. Corso, and P. Giannozzi, Rev. Mod. Phys. **73**, 515 (2001).
[72] O. Gomis, R. Vilaplana, F. J. Manjon, D. Santamaria-Perez, D. Errandonea, E. Perez-Gonzalez, J. Lopez-Solano, P. Rodriguez-Hernandez, A. Munoz, I. M. Tiginyanu, and V. V. Ursaki, Mater. Res. Bull. **48**, 2128 (2013).
[73] A. Grzechnik, V. V.Ursaki, K. Syassen, I. Loa, I. M.Tiginyanu, and M. Hanfland, J. Sol. St. Chem. **160**, 205 (2001).
[74] S. Meenakshi, V. Vijayakumar, A. Eifler, and H. D. Hochheimer, J. Phys. Chem. Sol. **71**, 832 (2010).
[75] S. Meenakshi, V. Vijyakumar, B. K. Godwal, A. Eifler, I. Orgzall, S. Tkachev, and H. D. Hochheimer, J. Phys. Chem. Sol. **67**, 1660 (2006).
[76] R. Vilaplana, M. Robledillo, O. Gomis, J. A. Sans, F. J. Manjon, E. Perez-Gonzalez, P. Rodriguez-Hernandez, A. Munoz, I. M. Tiginyanu, and V. V. Ursaki, J. Appl. Phys. **113**, 093512 (2013).
[77] J. Paier, R. Asahi, A. Nagoya, and G. Kresse, Phys. Rev. B **79**, 115126 (2009).
[78] C. Persson, J. Appl. Phys. **107**, 053710 (2010).
[79] S. Ahn, S. Jung, J. Gwak, A. Cho, K. Shin, K. Yoon, D. Park, H. Cheong, and J. H. Yun, Applied Physics Letters **97** (2010).
[80] G. Gordillo, C. Calderon, and P. Bartolo-Perez, Appl. Surf. Sci. **35**, 506 (2014).
[81] C.-R. Li, Y.-F. Li, B. Yao, G. Yang, Z.-H. Ding, R. Deng, and L. Liu, Phys. Lett. A **377**, 2398 (2013).
[82] A. Mujica, A. Rubio, A. Munoz, and R. J. Needs, Rev. Mod. Phys. **75**, 863 (2003).
[83] V. S. Bhadram, L. Krishna, E. S. Toberer, R. Hrubiak, E. Greenberg, V. B. Prakapenka, and T. A. Strobel, Appl. Phys. Lett. **110**, 182106 (2017).
[84] O. Gomis, D. Santamaria-Perez, R. Vilaplana, R. Luna, J. A. Sans, F. Manjon, D. Errandonea, E. Perez-Gonzalez, P. Rodriguez-Hernandez, A. Munoz, I. M. Tiginyanu, and V. V. Ursaki, J. Alloys Comp. **583**, 70 (2013).
[85] O. Gomis, R. Vilaplana, F. J. Manjon, E. Perez-Gonzalez, J. Lopez-Solano, P. Rodriguez-Hernandez, A. Munoz, D. Errandonea, J. Ruiz-Fuertes, A. Segura, D. Santamaria-Perez, I. M. Tiginyanu, and V. V. Ursaki, J. Appl. Phys. **111**, 013518 (2012).
[86] O. Gomis, R. Vilaplana, F. J. Manjon, D. Santamaria-Perez, D. Errandonea, E. Perez-Gonzalez, J. Lopez-Solano, P. Rodriguez-Hernandez, A. Munoz, I. M. Tiginyanu, and V. V. Ursaki, J. Appl. Phys. **113**, 073510 (2013).

[87] F. J. Manjon and R. I. Vilaplana, *Pressure-Induced Phase Transitions in AB2X4 Chalcogenide Compounds*, edited by F. J. Manjon, I. Tiginyanu, and V. V. Ursaki (Springer-Verlag Berlin Heidelberg, 2014).

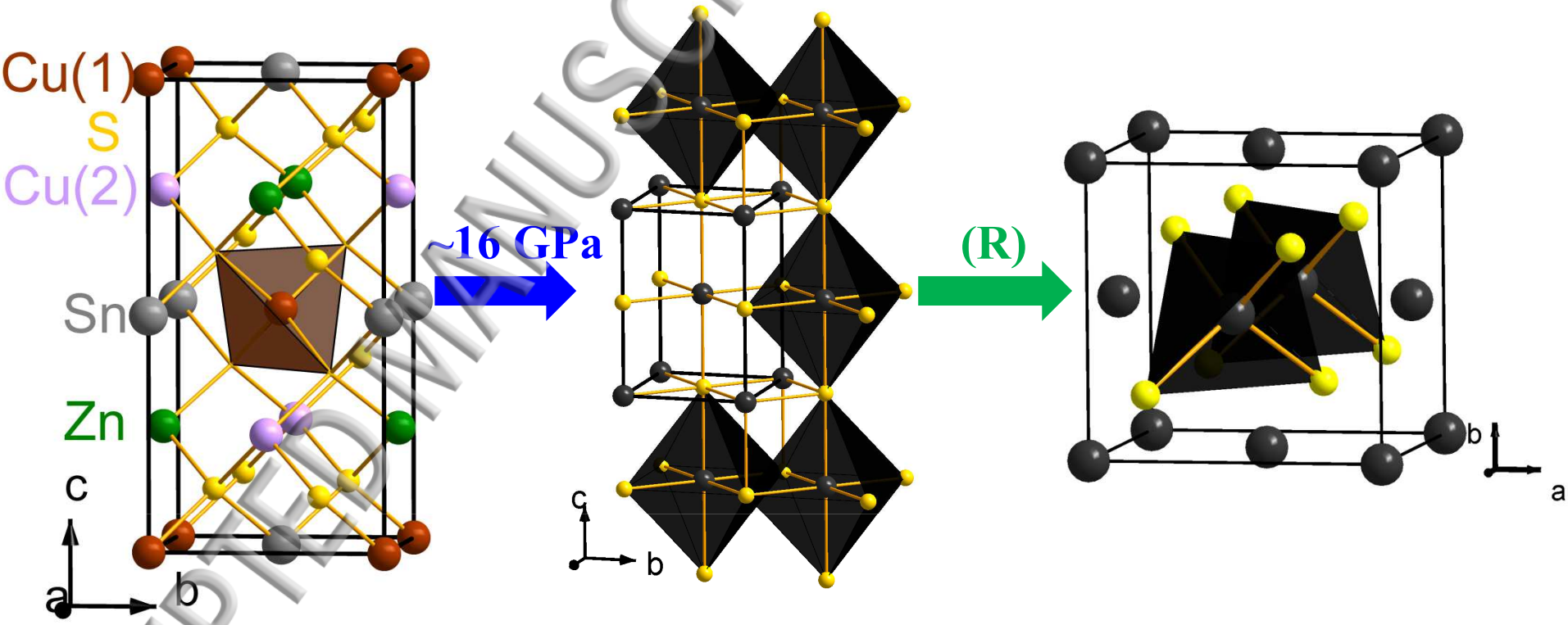
Cu(1)
S
Cu(2)
Sn
Zn
c
a
b
~16 GPa
c
b
(R)
b
a

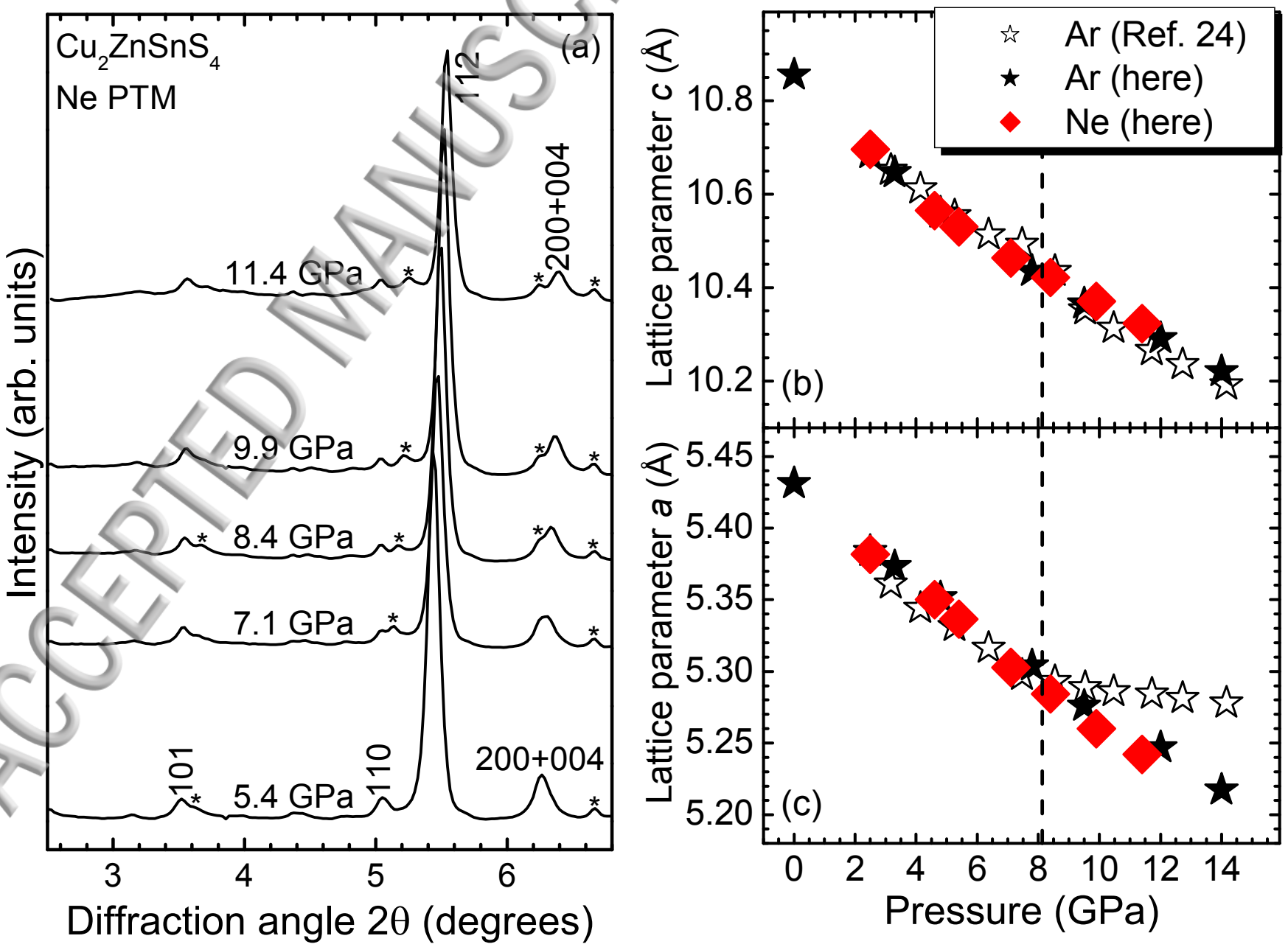

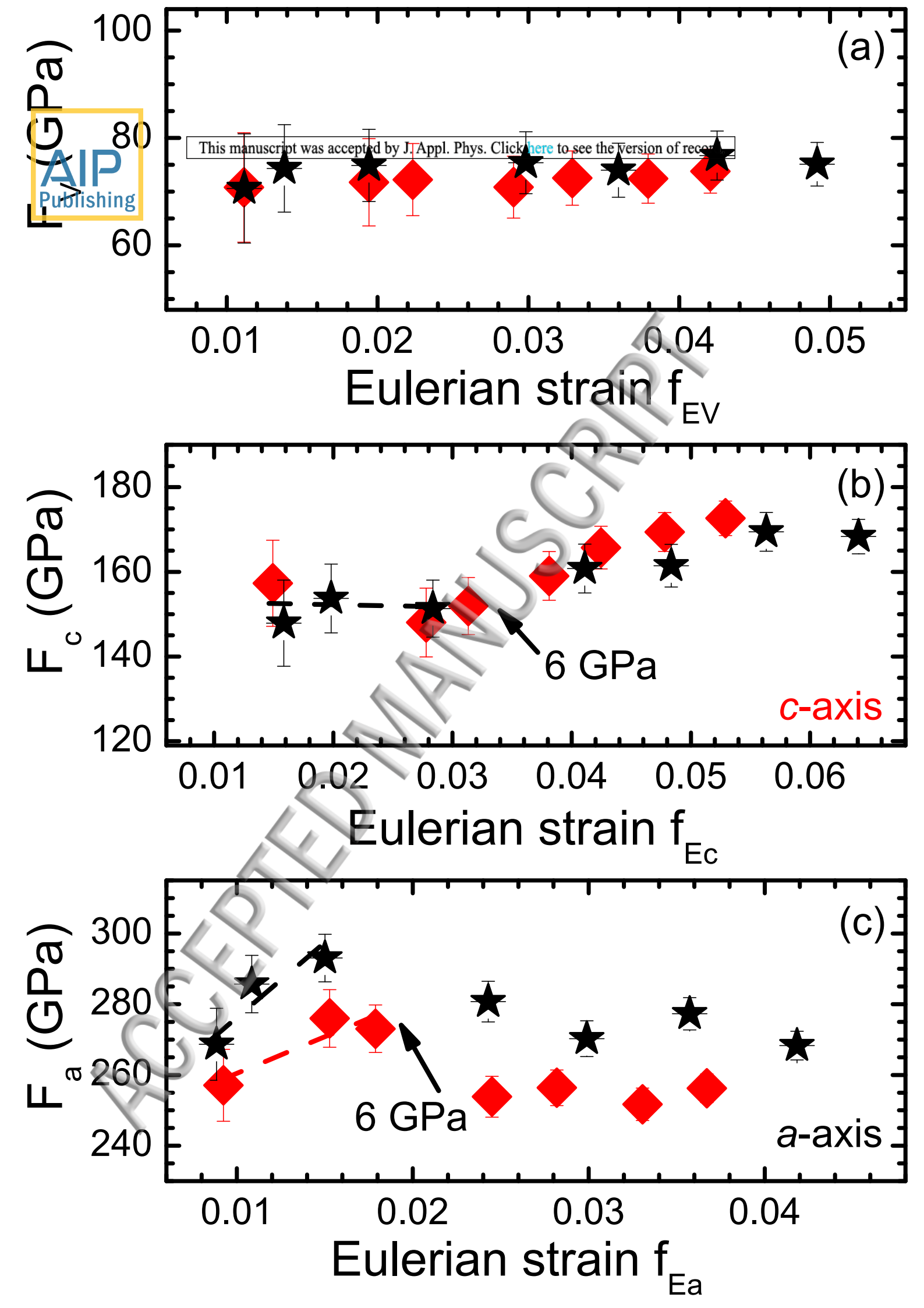

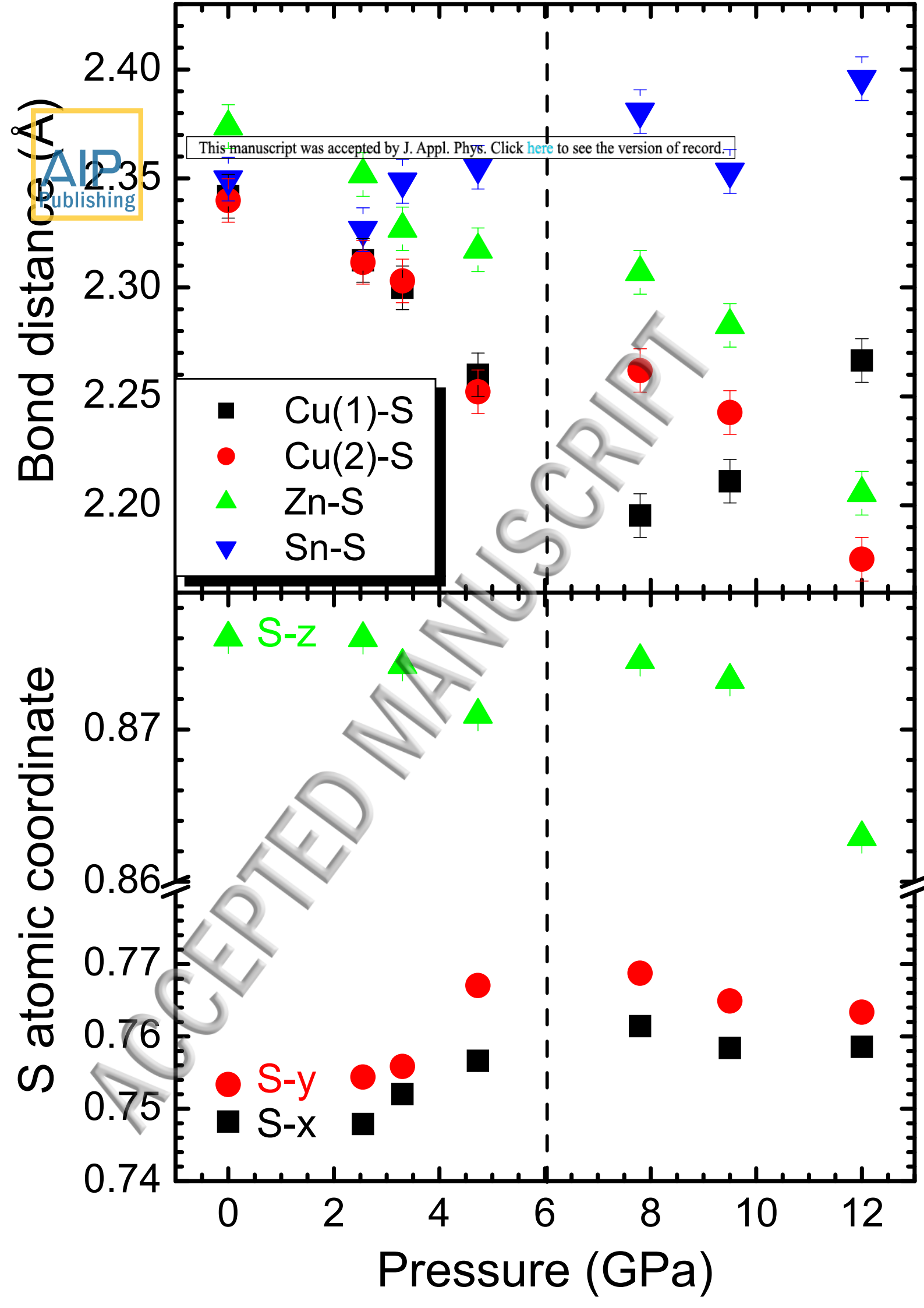

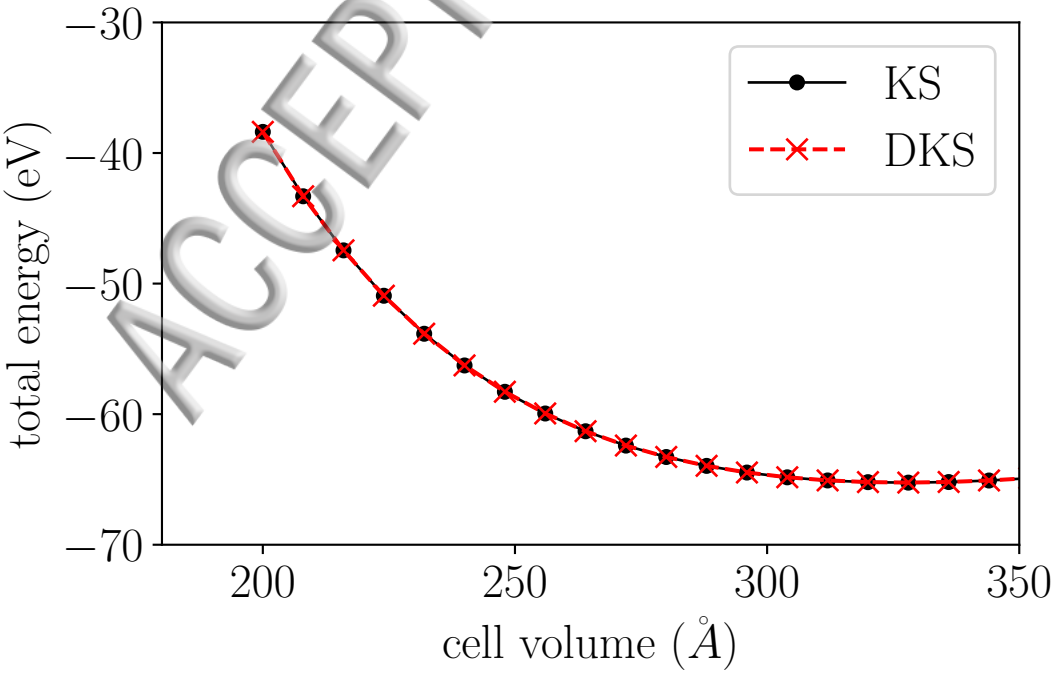
−30
−40
−50
−60
−70
total energy (eV)
200
250
300
350
cell volume ($\AA$)
KS
DKS

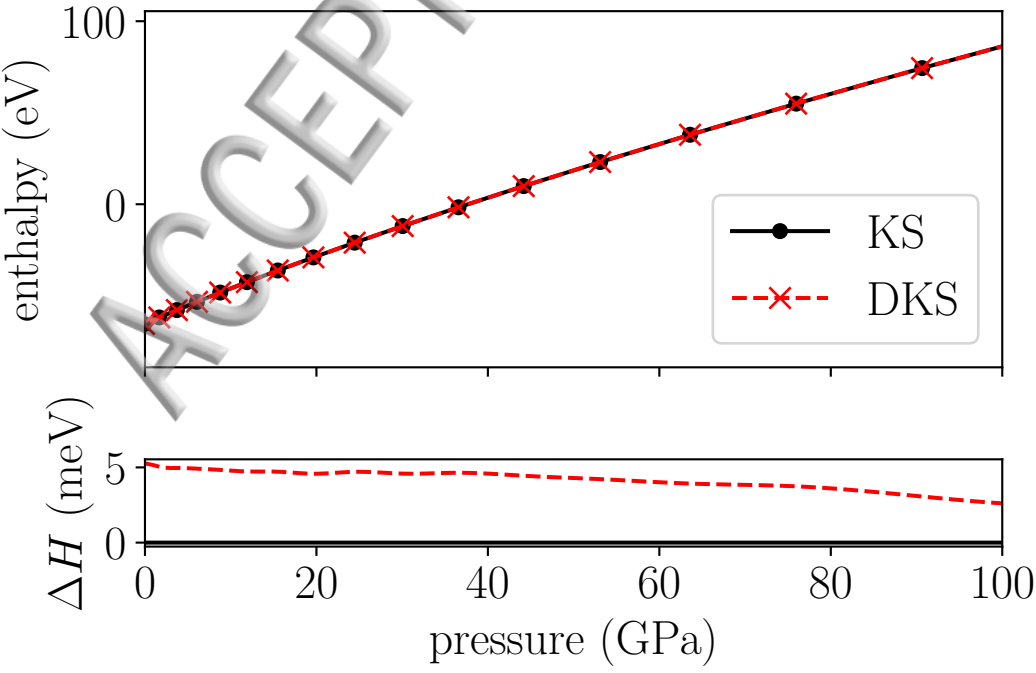
100
0
enthalpy (eV)
KS
DKS
5
0
ΔH (meV)
0
20
40
60
80
100
pressure (GPa)

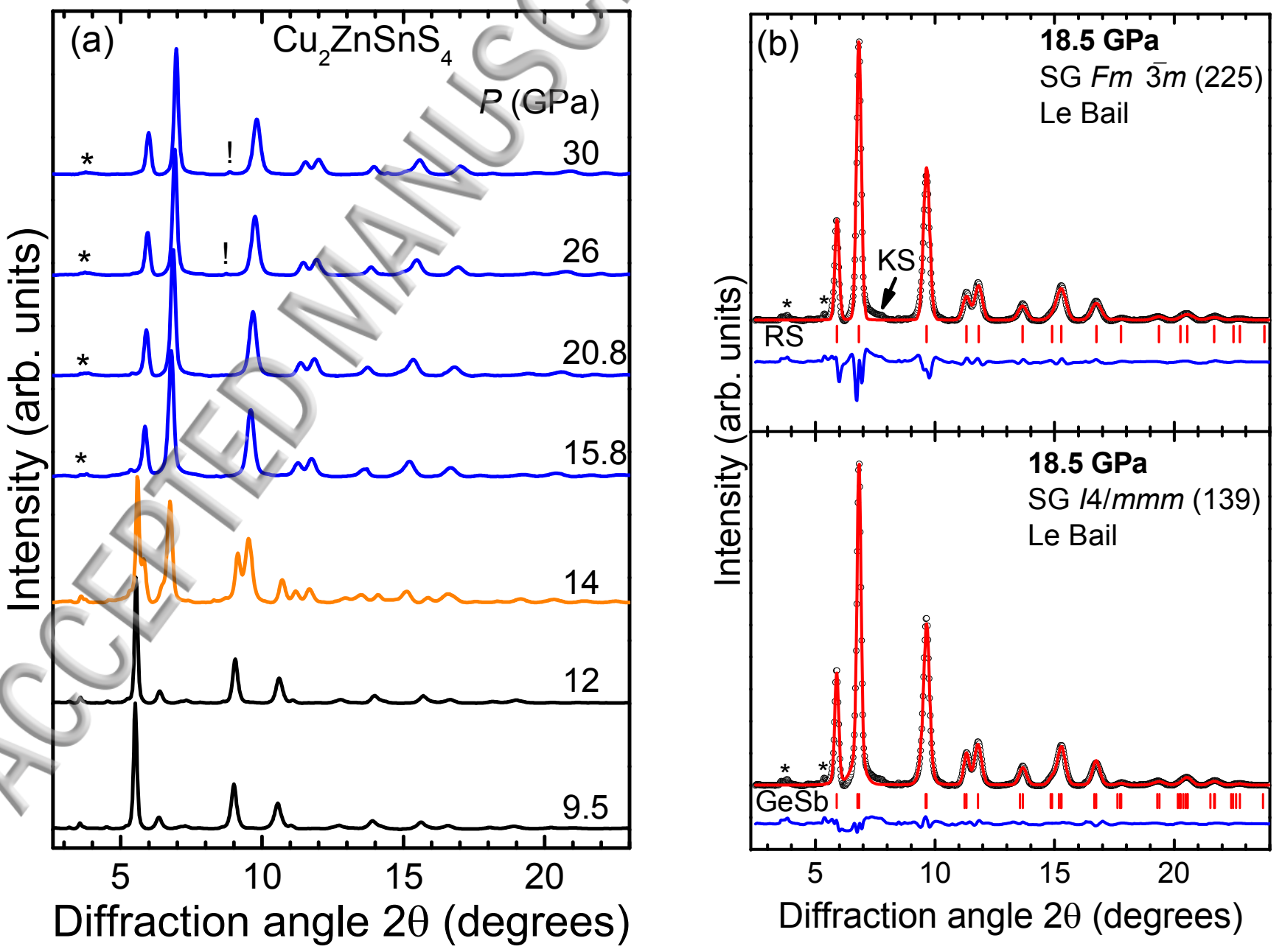

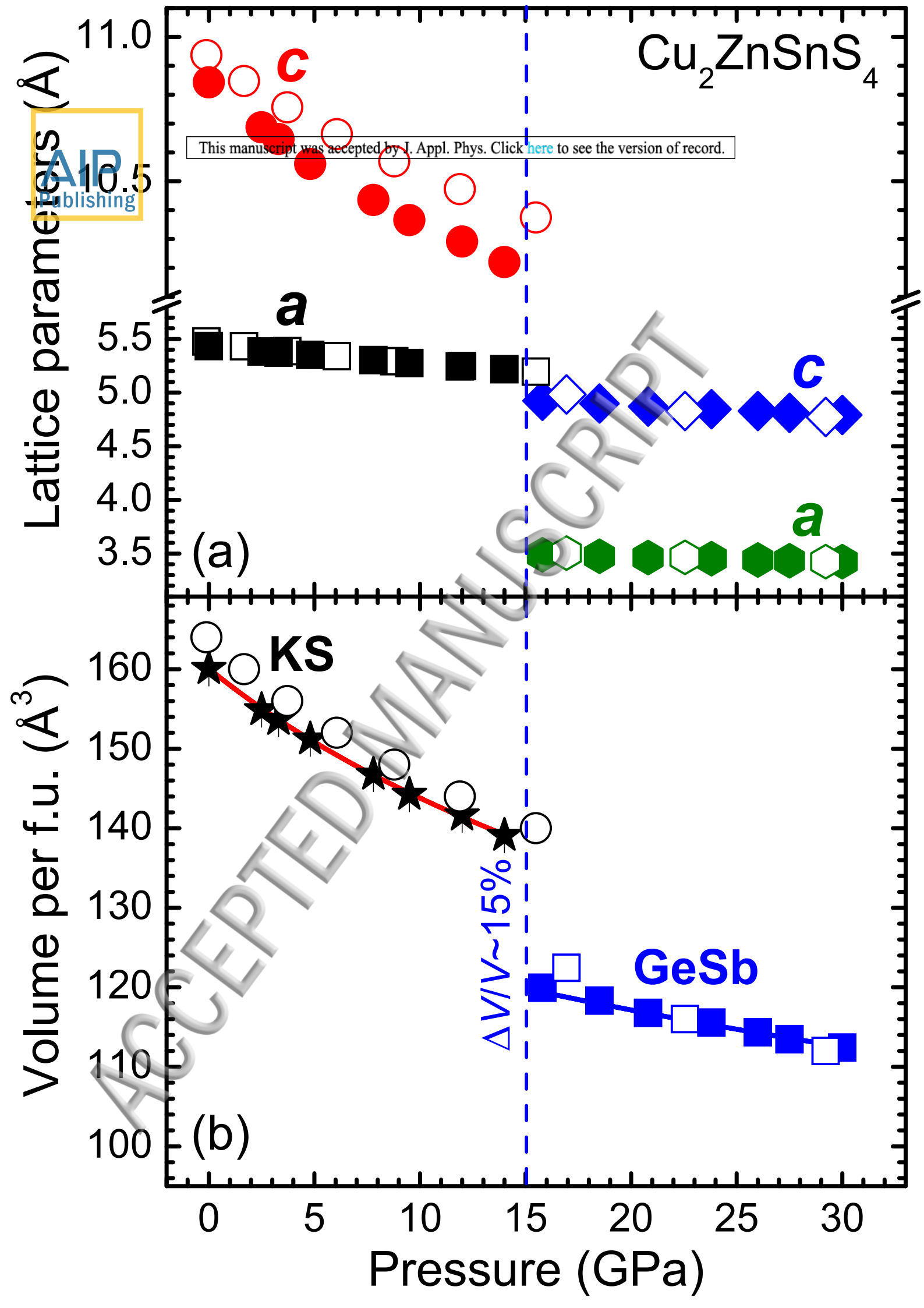

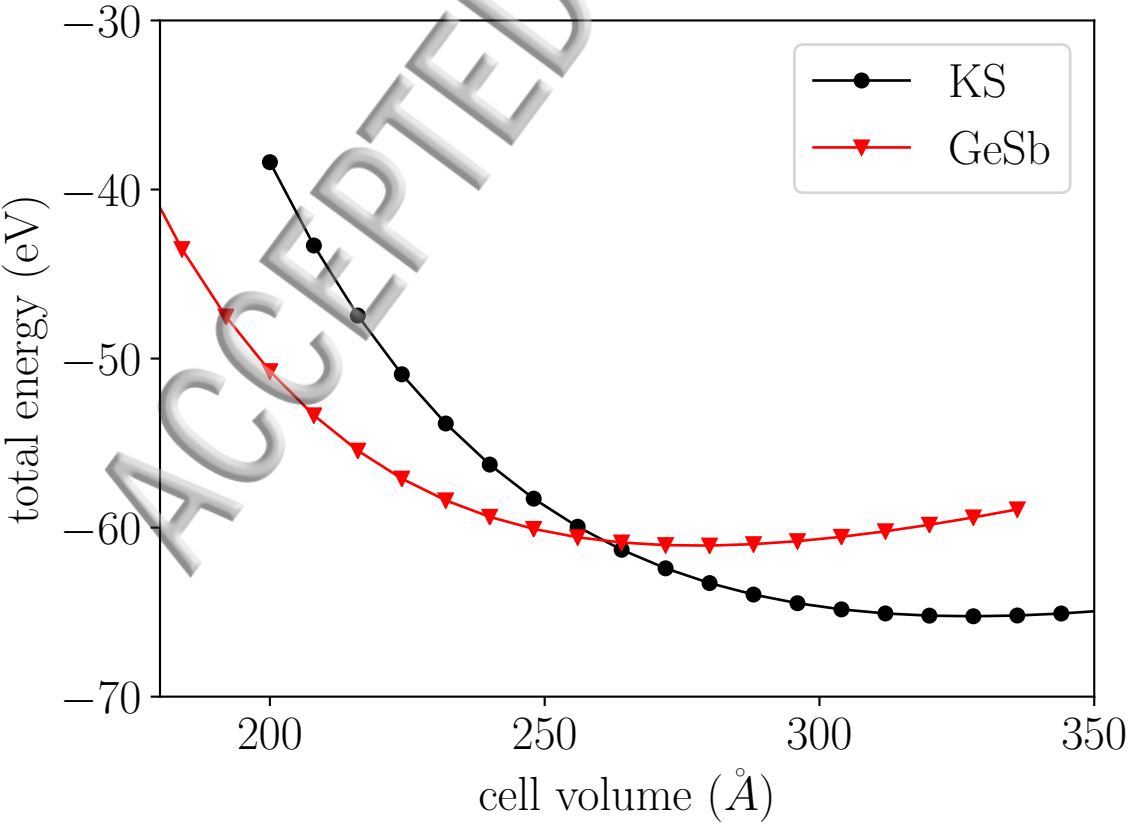
−30
−40
−50
−60
−70
total energy (eV)
200
250
300
350
cell volume ($\AA$)
KS
GeSb

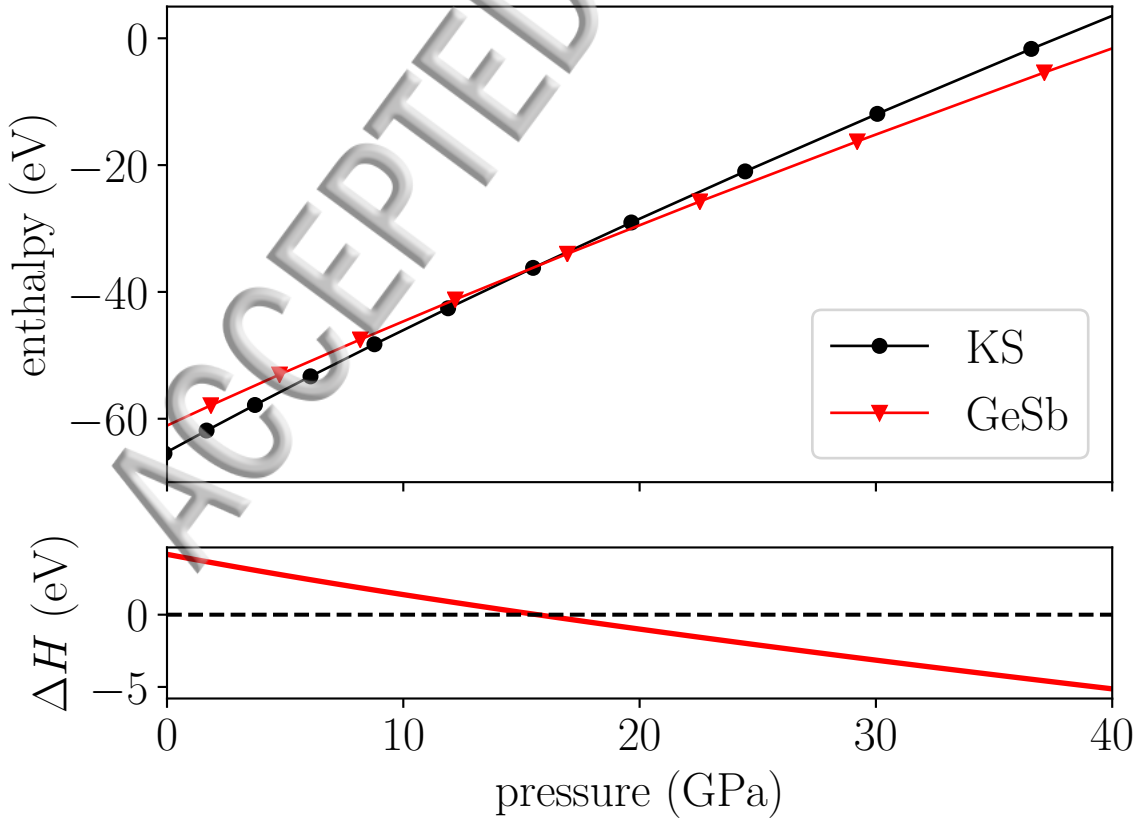
0
−20
−40
−60
enthalpy (eV)
KS
GeSb
ΔH (eV)
0
−5
0
10
20
30
40
pressure (GPa)

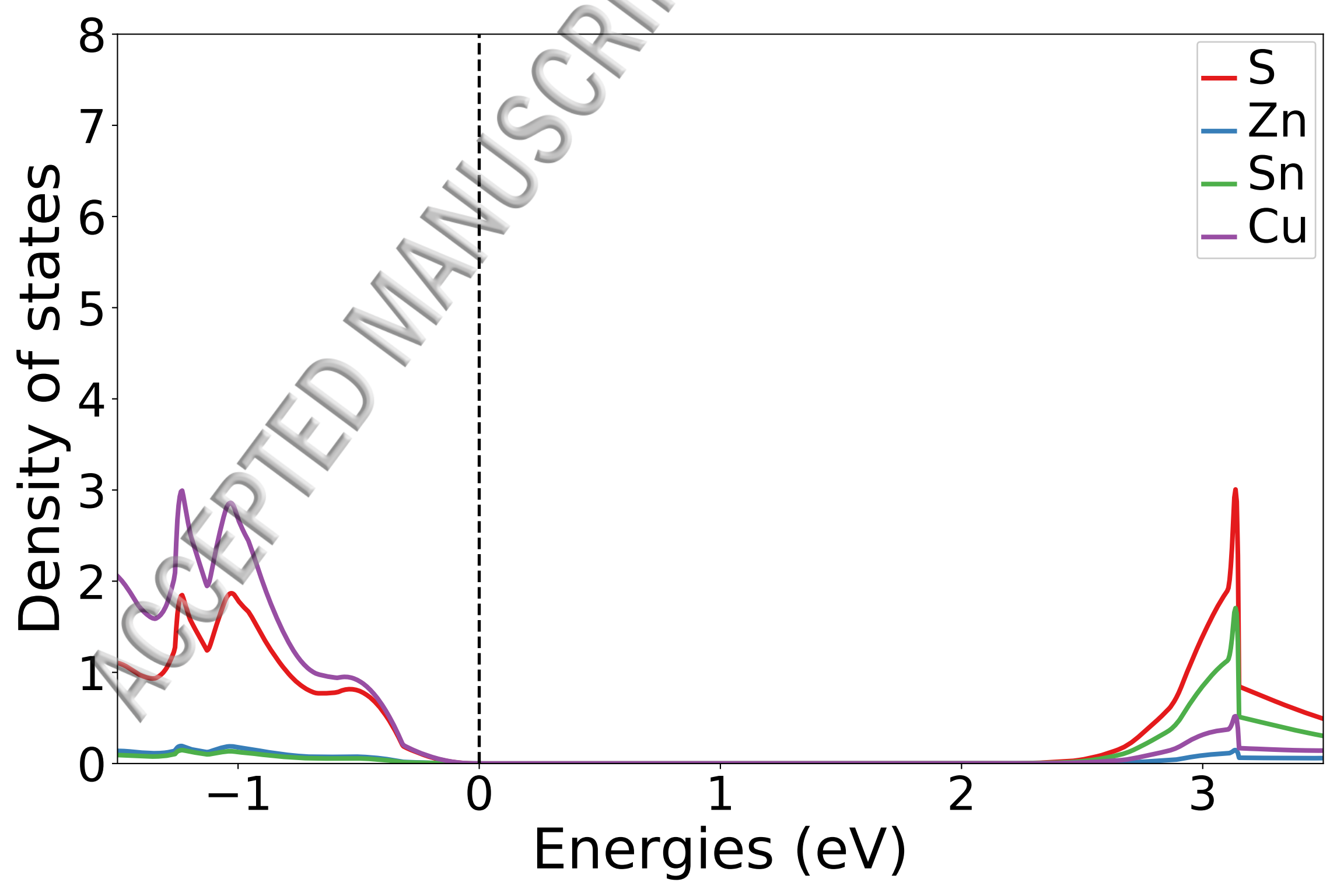

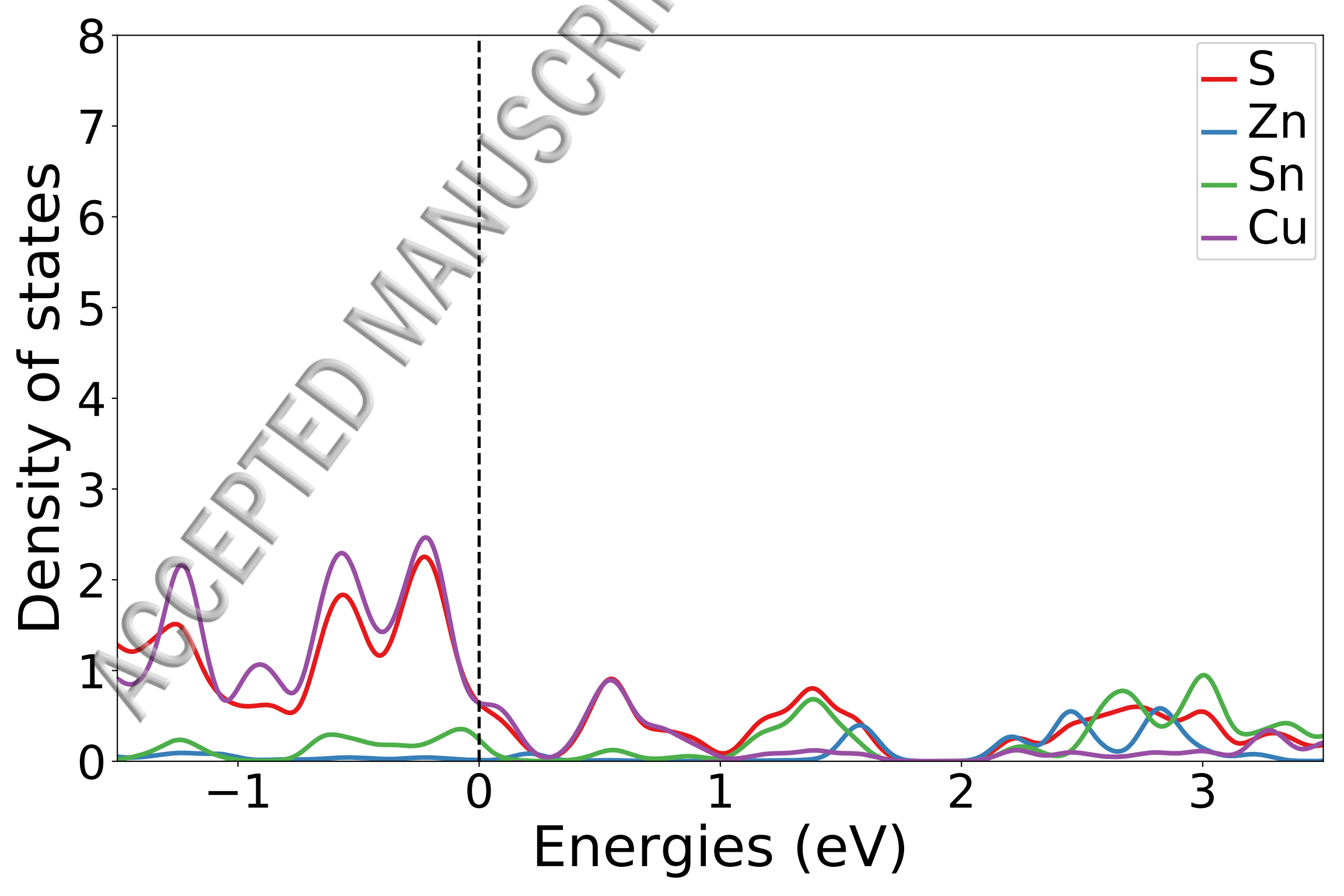

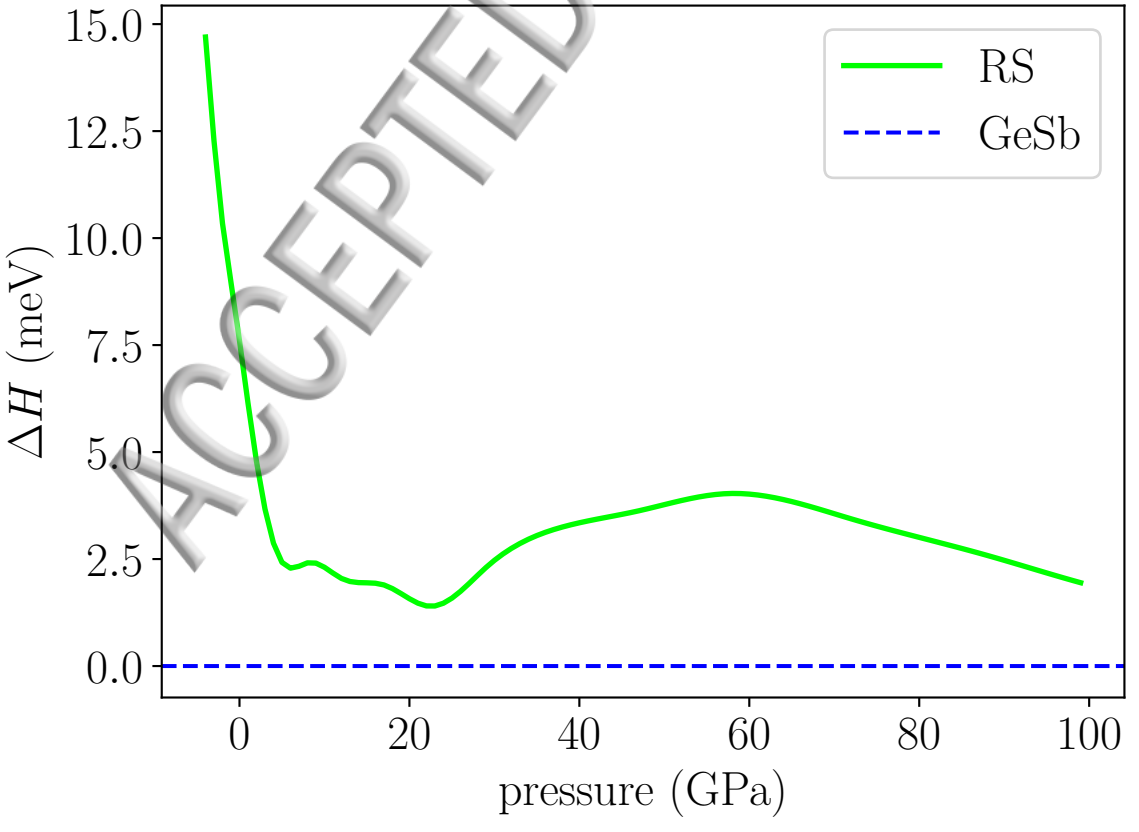
15.0
12.5
10.0
7.5
5.0
2.5
0.0
ΔH (meV)
0
20
40
60
80
100
pressure (GPa)
RS
GeSb